Mon. Not. R. Astron. Soc. **000**, 1–30 (2015) Printed 1 March 2024 (MN LATEX style file v2.2)

A new multidimensional, energy-dependent two-moment transport code for neutrino-hydrodynamics

O. Just,[1,2] M. Obergaulinger,[3] and H.-T. Janka[1]
[1] *Max-Planck-Institut für Astrophysik, Postfach 1317, 85741 Garching, Germany*
[2] *Max-Planck/Princeton Center for Plasma Physics (MPPC)*
[3] *Departament d´Astronomia i Astrofísica, Universitat de València, Edifici d´Investigació Jeroni Muñoz, C/ Dr. Moliner, 50, E-46100 Burjassot (València), Spain*

Released 2015 Xxxxx XX

ABSTRACT

We present the new code ALCAR developed to model multidimensional, multi energy-group neutrino transport in the context of supernovae and neutron-star mergers. The algorithm solves the evolution equations of the 0th- and 1st-order angular moments of the specific intensity, supplemented by an algebraic relation for the 2nd-moment tensor to close the system. The scheme takes into account frame-dependent effects of order $\mathcal{O}(v/c)$ as well as the most important types of neutrino interactions. The transport scheme is significantly more efficient than a multidimensional solver of the Boltzmann equation, while it is more accurate and consistent than the flux-limited diffusion method. The finite-volume discretization of the essentially hyperbolic system of moment equations employs methods well-known from hydrodynamics. For the time integration of the potentially stiff moment equations we employ a scheme in which only the local source terms are treated implicitly, while the advection terms are kept explicit, thereby allowing for an efficient computational parallelization of the algorithm. We investigate various problem setups in one and two dimensions to verify the implementation and to test the quality of the algebraic closure scheme. In our most detailed test, we compare a fully dynamic, one-dimensional core-collapse simulation with two published calculations performed with well-known Boltzmann-type neutrino-hydrodynamics codes and we find very satisfactory agreement.

Key words: radiative transfer - neutrinos - hydrodynamics - supernovae - neutron stars

1 INTRODUCTION

In various astrophysical scenarios involving matter in a hot and dense phase, neutrino interactions take place in a way that the full transport problem – which consistently follows the emission, propagation and absorption of neutrinos – needs to be taken into account to correctly describe these systems. A prominent example is a core-collapse supernova (CCSN), in which according to the present standard model the explosion is essentially only made possible by the energy deposition due to the re-absorption of neutrinos just produced in the proto-neutron star (proto-NS; see Janka 2012; Burrows 2013 for recent reviews). Genuine neutrino-transport effects can also be crucial for determining the properties of potentially nucleosynthesis-relevant outflows and may even give rise to these outflows to begin with. Such outflows are believed to occur during a CCSN in the form of a neutrino-driven wind expelled from the surface of the proto-NS (e.g. Qian & Woosley 1996). Another example is a massive NS formed during the merger of two NSs (Dessart et al. 2009), or similarly a black-hole (BH) torus configuration also produced by such a merger or by the merger of a NS and a BH (e.g Wanajo & Janka 2012; Fernández & Metzger 2013). Another astrophysical scenario in which neutrino transport may be crucial is the launching of a gamma-ray burst jet, which could be powered to some degree by neutrino pairs annihilating in the polar regions of a BH-torus system (e.g. Popham et al. 1999).

Unfortunately, most multidimensional results for the aforementioned scenarios stem from more or less idealized investigations, mainly owing to the enormous computational requirements of a time-dependent, multidimensional treatment of neutrino transport. The level of simplification is typically chosen to provide the optimal balance between accuracy and computational expense, given the constraints of the available computational resources and the considered physical effects to be captured to a sufficient degree. The most accurate neutrino-transport schemes follow the full spatial, energetic and directional dependence of the neutrino dis-

tribution, described by the Boltzmann equation. However, multidimensional applications of these "Boltzmann solvers" are severely constrained by their complexity and computational expense and force modern simulations to employ miscellaneous restrictions, such as the "ray-by-ray" approach (e.g. Buras et al. 2006; Hanke et al. 2012), the omission of (a subset of) velocity-dependent terms and the decoupling of neutrinos with different energies (e.g. Livne et al. 2004; Ott et al. 2008), or the investigation of only individual static background configurations of matter (Sumiyoshi et al. 2015). A computationally cheaper alternative to a Boltzmann solver is the "flux-limited diffusion" (FLD) method (see, e.g., Levermore & Pomraning 1981; Mihalas & Mihalas 1984), in which the radiation energy density (as represented by the 0th angular moment of the specific intensity, see Sec. 2 for explicit definitions) is evolved assuming that the radiation flux density (as represented by the 1st angular moment) can be written as a function of the radiation energy density. This method is the simplest realization of a "truncated moment scheme". However, FLD implies several physical as well as technical drawbacks.

In this paper we present a genuinely multidimensional, fully energy-dependent radiation-hydrodynamics (RHD) scheme where both the energy density and the flux density of neutrinos are evolved quantities. The system of equations is closed by an algebraic expression for the Eddington tensor (defined as the normalized 2nd angular moment of the specific intensity) as function of the lower-order moments. This makes the scheme a specific realization of the class of "variable Eddington factor" methods and it will therefore be denoted here as "algebraic Eddington factor" (AEF) method.

In both methods, AEF and FLD, the closure (i.e. the corresponding angular moment which closes the set of moment equations) is assumed to be given solely as a function of the local values of the evolved radiation moments (or additionally of the local gas properties in the case of FLD). Since in general the closure is a non-local function of the surrounding radiation sources, it is clear that a universal closure relation between the local angular moments, corresponding to an equation of state as in hydrodynamics, does not exist for arbitrarily shaped radiation fields. It is nevertheless conceivable that for not too complex geometries (e.g. single-source configurations like a PNS or a NS-merger remnant) the radiation field tends to be arranged such that typical relations between the lowest angular moments are fulfilled up to a sufficient degree. Keeping also in mind that not the full angular information but rather only the angular moments of the radiation field enter the hydrodynamics part of the full RHD system, the fluid may only be secondarily affected by the error introduced by the approximate closure. Certainly, the actual performance and applicability of either method, FLD or AEF, is problem dependent and has to be examined individually for a given problem setup. However, the main advantage of an AEF scheme (and also of an FLD scheme) compared to a more accurate Boltzmann solver is its computational efficiency, which allows to perform genuinely multidimensional RHD simulations and larger sets of model calculations with reasonable computational effort in the first place.

Compared to a standard FLD solver, the AEF method as presented in this paper features the following advantages: (1) It is potentially more accurate, simply on account of the fact that an FLD scheme is essentially an AEF scheme in which a certain collection of terms is dropped (e.g. Levermore & Pomraning 1981; Cernohorsky & van den Horn 1990; Dgani & Cernohorsky 1991). (2) It is more consistent: A particular consequence of retaining the evolution equations for the 1st moments in AEF is that the conservation of the total (radiation plus fluid) momentum and therefore also of the total energy can be ensured in the case of momentum-exchanging interactions between neutrinos and the gas (Baron et al. 1989; Cernohorsky & van den Horn 1990). Another, related advantage is that the 1st-moment vectors can in principle point into arbitrary directions in an AEF scheme and are not forced to be parallel to the gradient of the 0th moments as in FLD. This allows, for example, to describe shadows behind illuminated opaque structures (see the test problem in Sec. 4.2.1). (3) The different mathematical nature of the evolution equations in AEF (hyperbolic as opposed to parabolic in FLD) enables the application of time-explicit methods based on Riemann-solvers for the advection part of the system. Such methods are well-known from hydrodynamics. In contrast, in a time-explicit treatment of FLD the time step would in principle be unbound from below, which in practice forces one to employ a fully time-implicit scheme. An explicit scheme compared to an implicit one is particularly advantageous in multidimensional simulations, however, because first, its computational requirements only scale linearly with the size of the grid, and second, the computational parallelization is generally more efficient and straightforward.

The strategy of using an AEF scheme for radiation transport is not new[1]. Multidimensional applications regarding photon transport exist in a number of realizations (see, e.g., Audit et al. 2002; Hayes & Norman 2003; González et al. 2007; Aubert & Teyssier 2008; Vaytet et al. 2011; Sądowski et al. 2013; Skinner & Ostriker 2013; McKinney et al. 2014). Until recently, however, only a few investigations considered the AEF scheme in the context of neutrino transport (Schinder & Bludman 1989; Dgani & Cernohorsky 1991; Koerner & Janka 1992; Cernohorsky & van Weert 1992) , although several studies concerning aspects of the closure prescription (Cernohorsky & Bludman 1994; Bludman & Cernohorsky 1995; Smit et al. 2000) and the solution strategies (Smit et al. 1997; Pons et al. 2000) elucidated its capabilities. In recent works by Shibata et al. (2011) and Cardall et al. (2013) the truncated two-moment scheme was extended to a general relativistic framework. Shibata & Sekiguchi (2012) made use of this framework in the "grey" approximation (i.e. averaging over the neutrino energies) and presented axisymmetric neutrino-magnetohydrodynamics simulations of BH accretion tori as models for central engines of gamma-ray bursts. Kuroda et al. (2012, 2014) combined the relativistic AEF scheme with an isotropic diffusion source approximation (IDSA, as developed in Liebendörfer et al. 2009) to perform three-dimensional CCSN simulations. A gen-

[1] In the literature, these schemes are sometimes simply denoted as "M_1 schemes", which actually only refers to the specific M_1 closure being used to express the Eddington tensor in a truncated two-moment scheme (see Sec. 2.4.2 for details).

eral relativistic AEF scheme was implemented in the GR1D code by O'Connor & Ott (2013), who conducted one-dimensional, energy-dependent CCSN simulations neglecting all velocity-dependent terms and energy-coupling interactions. Recently, O'Connor (2014) released an improved version of this scheme, including velocity-dependent terms and energy-coupling interactions, but still constrained to spherical symmetry. Another implementation of the AEF scheme, in special relativity and using a grey approximation, was presented in Takahashi et al. (2013).

In contrast to the schemes used in the aforementioned studies, the neutrino-transport code presented here, which will be designated the name "ALCAR" (**A**lgebraic **L**ocal **C**losure **A**pproach for **R**adiation), combines all of the following features: It is genuinely multidimensional, fully energy dependent and it takes into account all velocity-dependent terms up to order $\mathcal{O}(v/c)$ as well as energy-coupling due to Doppler shift and inelastic neutrino-matter interactions. To validate the numerical implementation of the algorithm and each of its aforementioned features we examine several test problems. However, the test problems are not only conducted to check the correct numerical implementation of the algorithm but also serve to examine the central approximation of the scheme embodied in the algebraic closure. In particular, two tests focus on the question how the AEF method performs in a CCSN setup and how sensitive the results are to specific choices of the closure. In one test problem, only the neutrino field is evolved in a fixed hydrodynamic background, making it possible to test the AEF scheme against the FLD and a Boltzmann scheme independently of the hydrodynamic treatment. In the other test problem, the results of a fully dynamic CCSN calculation are compared with results published in Liebendörfer et al. (2005), which were obtained with the two well-established Boltzmann-RHD codes VERTEX-PROMETHEUS (Rampp & Janka 2002) and AGILE-BOLTZTRAN (Liebendörfer et al. 2004). Our main findings from these tests are that the AEF scheme is sufficiently accurate to represent a competitive, though computationally much simpler, alternative to Boltzmann solvers in simulations of CCSNe. Note that this conclusion is in agreement with O'Connor (2014), who conducted a similar comparison between 1D CCSN simulations performed with his general relativistic AEF code and with the two aforementioned Boltzmann codes.

This article is structured as follows: In Sec. 2, we outline the steps that lead from the equation of radiative transfer to the moment equations that are solved in our code, and we motivate and present the approximations and assumptions contained in the AEF method. Subsequently, in Sec. 3, we describe the methods used to discretize the moment equations in space, energy and time. In Sec. 4, we present a suite of test problems, in which we investigate the quality of the AEF approximation and study features such as the velocity dependence, the correct behavior in the static and dynamic diffusion limits, and the ability of the scheme to describe radiation shadowing. Finally, in Sec. 5 we summarize our presentation.

The conventions regarding our notation are as follows: We use lower-case, italic letters $i, j, k \ldots$ to denote spatial tensor components, lower-case roman letters $\mathsf{i}, \mathsf{j}, \mathsf{k} \ldots$ for grid indices and n for the time index. Moreover, we make use of the Einstein notation to write sums of products of tensor components. Symbols with hats, as for instance $\hat{X}$, refer to discretized quantities, while symbols with bars, as for instance $\bar{X}$, denote versions of the corresponding quantities integrated over the whole energy spectrum. Vectors in spatial and momentum space are denoted as $\boldsymbol{x}$ and $\boldsymbol{p}$, and t refers to the time coordinate. The symbols c, h and k_B mean the speed of light, the Planck constant and the Boltzmann constant, respectively.

2 THE $\mathcal{O}(V/C)$ EQUATIONS OF RADIATION HYDRODYNAMICS

In this section we briefly define the basic quantities and present the RHD equations used in our code.

2.1 The equation of radiative transfer in the comoving frame

Both the equations of hydrodynamics and of radiative transfer have their origin in the Boltzmann equation for the corresponding particle distribution function $\mathcal{F}$, in terms of which

$$\mathrm{d}N \;=\; \frac{g}{h^3}\mathcal{F}(\boldsymbol{x},\boldsymbol{p},t)\mathrm{d}^3x\,\mathrm{d}^3p \tag{1}$$

is the number of particles within the phase-space volume $\mathrm{d}^3x\,\mathrm{d}^3p$, where g is the statistical weight of the species. "Radiation" in the present context is defined as a distribution of particles that move with the speed of light c and that are not subject to an external force in an inertial frame ($\dot{\boldsymbol{p}} \equiv 0$). The Boltzmann equation for radiative transfer in a fixed frame then becomes ($\boldsymbol{n} \equiv \boldsymbol{p}/|\boldsymbol{p}|$):

$$\frac{1}{c}\frac{\partial}{\partial t}\mathcal{F} + \boldsymbol{n}\cdot\nabla_{\boldsymbol{x}}\mathcal{F} \;=\; \mathcal{B}\,. \tag{2}$$

Here, and in several following cases, we suppress the functional dependencies. The collision integral $\mathcal{B} \equiv \mathcal{B}(\boldsymbol{x},\boldsymbol{p},t)$ generally contains explicit integrals in momentum space, making Eq. (2) an integro-partial differential equation. Instead of working with the distribution function directly, for the macroscopic view one prefers using the frame-dependent specific (i.e. monochromatic) intensity

$$\mathcal{I}(\boldsymbol{x},\boldsymbol{n},\epsilon,t) = (\epsilon/hc)^3\,c\,\mathcal{F}(\boldsymbol{x},\boldsymbol{p},t)\,, \tag{3}$$

where[2] $\epsilon = |\boldsymbol{p}|c$. Bearing in mind that an essential part of the collision integral depends on the distributions of fluid particles it is often preferable to measure $\mathcal{I}$ in the frame comoving with the fluid ("comoving frame", "fluid frame"), since in that frame the isotropy of the fluid particle distributions[3] induces symmetries in the collision integral that make it computationally most feasible. Using arbitrary, but fixed, Eulerian spatial coordinates defined in a frame we denote as the laboratory frame ("lab-frame") and momentum space coordinates (i.e. ϵ and $\boldsymbol{n}$) defined in the fluid frame, the comoving-frame equation of radiative transfer up to order $\mathcal{O}(v/c)$ ($v \equiv |\boldsymbol{v}|$ is the velocity of the fluid as measured

[2] We will use the terms "energy" and "frequency" interchangeably when referring to the corresponding degree of freedom in phase space.

[3] We implicitly assume the fluid to be in local thermodynamic equilibrium (but not necessarily in equilibrium with neutrinos).

in the lab frame) becomes (e.g. Buchler 1979; Kaneko et al. 1984; Munier & Weaver 1986):

$$\begin{aligned}
&\frac{1}{c}\frac{\partial\mathcal{I}}{\partial t}+\frac{\boldsymbol{v}\cdot\boldsymbol{n}}{c^2}\frac{\partial\mathcal{I}}{\partial t}+n^j\frac{\partial\mathcal{I}}{\partial x^j}+\frac{v^j}{c}\frac{\partial\mathcal{I}}{\partial x^j}\\
&+\frac{\partial}{\partial\epsilon}\left[\mathcal{I}\epsilon\left(\frac{\boldsymbol{a}\cdot\boldsymbol{n}}{c^2}+\frac{1}{c}n^jn^k\nabla_jv_k\right)\right]\\
&+\frac{\partial}{\partial n^i}\left[\mathcal{I}\left(\frac{\boldsymbol{a}\cdot\boldsymbol{n}}{c^2}n^i-\frac{a^i}{c^2}+\frac{1}{c}n^in^jn^k\nabla_jv_k-\frac{1}{c}n^j\nabla_jv^i\right.\right.\\
&\qquad\left.\left.-\Gamma^i_{jk}n^jn^k-\frac{1}{c}\Gamma^i_{jk}v^jn^k\right)\right]\\
&+\mathcal{I}\left[2\frac{\boldsymbol{a}\cdot\boldsymbol{n}}{c^2}+\frac{1}{c}\nabla_iv^i+\Gamma^i_{ij}n^j+\frac{1}{c}n^in^j\nabla_iv_j\right]=\mathcal{C}\,, \quad (4)
\end{aligned}$$

where $\boldsymbol{a}\equiv\partial_t\boldsymbol{v}$, Γ^i_{jk} are the Christoffel symbols associated with the spatial coordinates and $\mathcal{C}\equiv(\epsilon/hc)^3c\mathcal{B}$. Equation (4) can be derived from Eq. (2) using Eq. (3) and the $\mathcal{O}(v/c)$ versions of the Lorentz transformations for $\mathcal{I}$, ϵ and $\boldsymbol{n}$.

2.2 Angular moments of the transfer equation

In order to reduce the dimensionality of the radiative transfer problem and to construct the link to the hydrodynamics equations, one utilizes the fact that the specific intensity is related to the specific (frequency-integrated) energy density E ($\bar{E}$), energy flux density F^i ($\bar{F}^i$) and pressure tensor P^{ij} ($\bar{P}^{ij}$) of radiation by virtue of its angular moments of increasing order, defined by

$$\{cE,F^i,cP^{ij},Q^{ijk}\}=\int\mathrm{d}\Omega\,\mathcal{I}\,\{1,n^i,n^in^j,n^in^jn^k\}\,, \quad (5)$$

and

$$\{\bar{E},\bar{F}^i,\bar{P}^{ij},\bar{Q}^{ijk}\}=\int\mathrm{d}\epsilon\,\{E,F^i,P^{ij},Q^{ijk}\}\,, \quad (6)$$

where Q^{ijk} and $\bar{Q}^{ijk}$ are the analog 3rd-moment quantities.

In the following, we neglect terms including the acceleration a^i and the second term containing the time derivative in Eq. (4). These terms are effectively of order $\mathcal{O}(v^2/c^2)$ for temporal changes of the velocity and radiation fields occuring on a fluid timescale l/v, where l is a characteristic length scale of changes in the hydrodynamic background and v a typical fluid velocity (Mihalas & Mihalas 1984; see, however, Rampp & Janka 2002 and Lowrie et al. 2001 for comments on the second term of Eq. (4)). Temporal changes of these fields on the radiation timescale l/c would enhance the importance of the aforementioned terms. In that case, however, the preceding validity assumption of the $\mathcal{O}(v/c)$ equation may become questionable to begin with anyway. It is worth noting that the results of one test in Sec. 4.3.2 suggest that for the conditions in CCSNe the omission of the aforementioned terms is justified.

2.2.1 Moment equations of energy transport

The system for the first two moments of Eq. (4), excluding the aforementioned terms that are effectively of order $\mathcal{O}(v^2/c^2)$, is obtained by performing the angular integrations as in Eq. (5) and it reads

$$\begin{aligned}
&\partial_tE+\nabla_jF^j+\\
&\quad\underbrace{\nabla_j(v^jE)}_{\text{(I)}}+\underbrace{(\nabla_jv_k)P^{jk}}_{\text{(II)}}-\underbrace{(\nabla_jv_k)\partial_\epsilon(\epsilon P^{jk})}_{\text{(IV)}}=C^{(0)}\,, \quad (7a)\\
&\partial_tF^i+c^2\nabla_jP^{ij}+\\
&\quad\underbrace{\nabla_j(v^jF^i)}_{\text{(I)}}+\underbrace{F^j\nabla_jv^i}_{\text{(III)}}-\underbrace{(\nabla_jv_k)\partial_\epsilon(\epsilon Q^{ijk})}_{\text{(IV)}}=C^{(1),i}\,, \quad (7b)
\end{aligned}$$

where $C^{(0)}\equiv\int\mathrm{d}\Omega\,\mathcal{C}$ and $C^{(1),i}\equiv\int\mathrm{d}\Omega\,n^i\,\mathcal{C}$. The labeling by Roman numerals denotes the different types of velocity-dependent terms: The (I)-terms account for the change of the comoving-frame moments owing to advection. The (II)-terms account for the change of radiation energy due to compressional work against the radiation pressure. The (III)-terms account for changes of the radiation fluxes due to aberration. The energy-coupling (IV)-terms are responsible for the change of the spectral shape of the radiation field associated with the Doppler shift. Note that in the grey formulation of the moment equations (i.e. after integrating Eqs. (7) over energy ϵ) the (IV)-terms vanish. For the explicit form of Eqs. (7) in spherical polar coordinates (additionally including the aforementioned terms that are omitted in our presentation) the reader may consult the Appendix of Buras et al. (2006).

Equations (7) are the radiation evolution equations used in our code. Since the source terms in general depend on the energy and species of neutrinos, we have to solve a set of moment equations for each energy group (after discretizing the energy space into a finite set of energy groups/bins, cf. Sec. 3) and for each species. Hence, given N_ϵ energy bins, $N_{\rm spe}$ species and taking into account $N_{\rm dim}$ components of the flux density F^i, we have to process $(N_{\rm dim}+1)\times N_{\rm spe}\times N_\epsilon$ equations in total in our multidimensional, multi-group radiation transport scheme. For the following presentation, however, we will only indicate individual species or the energy dependence if it is demanded by the context.

2.2.2 Moment equations of number transport

The moments connected to the number transport (number density, number flux density etc.) are given by

$$\{\,N,F^i_N,P^{ij}_N,Q^{ijk}_N,\dots\,\}\equiv\epsilon^{-1}\{\,E,F^i,P^{ij},Q^{ijk},\dots\,\}. \quad (8)$$

Although we do not directly use them in our code, we list the equations describing the neutrino number evolution for completeness here. They are structurally similar to Eqs. (7) except for terms associated with the energy derivatives:

$$\begin{aligned}
&\partial_tN+\nabla_jF^j_N+\nabla_j(v^jN)-\nabla_jv_k\partial_\epsilon(\epsilon P^{jk}_N)=\epsilon^{-1}C^{(0)}\,, \quad (9a)\\
&\partial_tF^i_N+c^2\nabla_jP^{ij}_N+\nabla_j(v^jF^i_N)+\\
&\quad F^j_N\nabla_jv^i-\nabla_jv_k\left[Q^{ijk}_N+\partial_\epsilon(\epsilon Q^{ijk}_N)\right]=\epsilon^{-1}C^{(1),i}\,. \quad (9b)
\end{aligned}$$

2.2.3 Transformation into lab-frame

The transformation of energy-integrated moments from the comoving into the lab-frame can be performed by referring to their intrinsic tensorial structure which dictates the way the Lorentz transformation has to be applied. The energy-associated moments $\bar{E},\bar{F}^i,\bar{P}^{ij}$ are components of a 2nd-rank

tensor, namely the energy–momentum tensor of radiation, while the number-associated 0th and 1st moments combine to a 4-vector. This results in the following transformation rules correct to order $\mathcal{O}(v/c)$ for the energy-related moments:

$$\bar{E}_{\rm lab} = \bar{E} + 2c^{-2}\, v_j \bar{F}^j \,, \tag{10a}$$

$$\bar{F}^i_{\rm lab} = \bar{F}^i + v^i \bar{E} + v_j \bar{P}^{ij} \,, \tag{10b}$$

$$\bar{P}^{ij}_{\rm lab} = \bar{P}^{ij} + \frac{1}{c^2}(v^i \bar{F}^j + v^j \bar{F}^i) \,, \tag{10c}$$

and for the number-related moments:

$$\bar{N}_{\rm lab} = \bar{N} + c^{-2}\, v_i \bar{F}^i_N \,, \tag{11a}$$

$$\bar{F}^i_{N,{\rm lab}} = \bar{F}^i_N + v^i \bar{N} \,. \tag{11b}$$

Note that these transformation rules only apply for the grey quantities but not for the monochromatic moments[4]. The energy-integrated source terms $\bar{C}^{(0)}, \bar{C}^{(1),i}$ transform into the lab-frame source terms $\bar{C}^{(0)}_{\rm lab}, \bar{C}^{(1),i}_{\rm lab}$ in a similar way as $\bar{N}$ and $\bar{F}_N$ (cf. Eq. (11)), i.e. as a 4-vector, since they are defined to form the right-hand side of a conservation law of a 2nd-rank tensor in its original relativistic formulation.

2.3 Interaction source terms and coupling to hydrodynamics

The interaction source terms are the actual terms that introduce the microphysical properties and the coupling of matter and radiation into the transport problem. The source terms $C^{(0)}, C^{(1),i}$ for the neutrino moments give rise to corresponding hydrodynamic source terms $Q_{\rm M}$, $Q_{\rm E}$ that account for the change of fluid momentum and gas internal energy, respectively, due to the interaction with neutrinos. We restrict ourselves here to the basic Euler equations and neglect additional physics, such as viscosity, magnetic fields or the co-evolution of a set of nuclear species. The evolution of the baryonic density ρ, momentum density ρv^i, total gas-energy density $e_{\rm t} \equiv e_{\rm i} + \rho \boldsymbol{v}^2/2$ (where $e_{\rm i}$ is the internal energy density) and electron fraction[5] Y_e is then dictated by the system

$$\partial_t \rho + \nabla_j(\rho v^j) = 0 \,, \tag{12a}$$

$$\partial_t(\rho Y_e) + \nabla_j(\rho Y_e v^j) = Q_{\rm N} \,, \tag{12b}$$

$$\partial_t(\rho v^i) + \nabla_j(\rho v^i v^j + P_{\rm g}) = Q^i_{\rm M} \,, \tag{12c}$$

$$\partial_t e_{\rm t} + \nabla_j \left(v^j (e_{\rm t} + P_{\rm g}) \right) = Q_{\rm E} + v_j Q^j_{\rm M} \,. \tag{12d}$$

The gas pressure $P_{\rm g}$ is obtained by invoking an equation of state (EOS), which at the same time provides the quantities required to compute the opacities (such as the temperature, chemical potentials, or particle densities in case of nuclear statistical equilibrium). By virtue of the physical meaning of the moments E and F^i, the source terms for the hydrodynamic equations can immediately be identified with

$$Q_{\rm E} = -\sum_{\rm species} \bar{C}^{(0)} \,, \tag{13a}$$

$$Q^i_{\rm M} = -\frac{1}{c^2} \sum_{\rm species} \bar{C}^{(1),i} \,, \tag{13b}$$

$$Q_{\rm N} = -m_{\rm B} \int_0^\infty \left[\left(\frac{C^{(0)}}{\epsilon} \right)_{\nu_e} - \left(\frac{C^{(0)}}{\epsilon} \right)_{\bar{\nu}_e} \right] {\rm d}\epsilon \,, \tag{13c}$$

where $m_{\rm B}$ is the atomic mass unit and the sums contain all contributions from individual neutrino species.

At present, the most important types of (electron-) neutrino interactions are implemented, namely the capture of (anti-) neutrinos and (anti-) electrons by free nucleons and nuclei, isoenergetic scattering of (anti-) neutrinos off free nucleons and nuclei, and inelastic scattering of (anti-) neutrinos off (anti-) electrons. All corresponding source terms are adopted as described in Rampp & Janka (2002), which is mostly based on the compilation given by Bruenn (1985).

For introducing further concepts in a way that keeps the presentation as essential as possible, in the following we will for simplicity assume that only isoenergetic scattering and absorption/emission reactions take place. In this case the source terms in the moment equations, Eqs. (7), can be written as (e.g. Bruenn 1985)

$$C^{(0)} = c\kappa_{\rm a} \left(E^{\rm eq} - E \right) \,, \tag{14a}$$

$$C^{(1),i} = -c(\kappa_{\rm a} + \kappa_{\rm s}) F^i \,, \tag{14b}$$

where $\kappa_{\rm a}$ and $\kappa_{\rm s}$ are the combined absorption (corrected for final-state Fermion-blocking) and scattering opacities, and $E^{\rm eq}$ is the equilibrium energy density associated with the Fermi-Dirac distribution $\mathcal{F}_{\rm FD}$,

$$\begin{aligned} E^{\rm eq}(\epsilon, \mu_\nu, T) &\equiv \int {\rm d}\Omega \left(\frac{\epsilon}{hc} \right)^3 \mathcal{F}_{\rm FD} \\ &\equiv \left(\frac{\epsilon}{hc} \right)^3 \frac{1}{\exp\{(\epsilon - \mu_\nu)/(k_{\rm B}T)\} + 1} \,, \end{aligned} \tag{15}$$

which is a function of the fluid temperature T and the chemical potential μ_ν of the corresponding neutrino species. The transport opacity $\kappa_{\rm tra}$, which is given by $\kappa_{\rm tra} = \kappa_{\rm a} + \kappa_{\rm s}$, is related to the mean free path λ_ν between two momentum-exchanging reactions via $\kappa_{\rm tra} = \lambda_\nu^{-1}$.

2.4 Algebraic closure methods

The full information contained in the Boltzmann equation can be captured equally well by an infinite series of conservation equations for the angular moments, in which the evolution equation for a moment of rank m contains the moment of rank $m+1$ within the divergence operator. Instead of solving the infinite series of moment equations, the series can be truncated at the level of the $(m+1)$-th moment, provided the $(m+1)$-th moment is available to close the set of m equations. However, in order to determine the $(m+1)$-th moment that is consistent with the Boltzmann equation, it is inevitable to solve the latter in some approximation or the other, using computationally expensive methods such as discrete ordinate or (long- or short-) characteristics schemes. A computationally much cheaper, though more approximate option is to assume that an algebraic closure relation holds

[4] However, corresponding $\mathcal{O}(v/c)$ expressions for the monochromatic moments can be formulated in terms of Taylor expansions of the moments in energy space (e.g. Mihalas & Mihalas 1984; Hubeny & Burrows 2007).

[5] As usual, this quantity is defined as $Y_e \equiv (n_{e^-} - n_{e^+})/n_{\rm B}$ with the number densities $n_{e^\pm}$ of electrons and positrons and the baryon number density $n_{\rm B}$.

between the evolved moments and the $(m+1)$-th moment. This is what defines the algebraic closure methods, such as FLD and AEF. Essentially, this corresponds to imposing additional conditions or symmetries on the local radiation field. The consequence is that two (out of seven in the general case) independent variables describing the angular dependence of the radiation field disappear from the treatment. Evidently, the tradeoff for this computational simplification is that an algebraic closure method may strongly vary in quality between different physical setups. For example, since in an algebraic closure method the consistent evolution of higher-order angular moments is ignored, it appears likely that the quality of the scheme appreciably depends on the geometric complexity of the radiation field, or equivalently on the shape and number of the individual radiation sources. Moreover, connected to this issue is the circumstance that in the optically thin limit of vanishing source terms an algebraic moment scheme is generally not able to accurately describe the unperturbed superposition of multiple radiation fronts, simply on account of the closure being a local, non-linear function of the evolved quantities. Despite these conceptual deficiencies, which have to be individually tested for in each case of application, algebraic closure methods can in many cases offer an excellent compromise between efficiency and accuracy when performing energy-dependent, multidimensional RHD simulations.

Independent of the rank at which the scheme is truncated, any closure prescription should agree with certain consistency requirements that directly follow from the definition of the moments or from the Boltzmann equation. Using the normalized moments $\boldsymbol{f} \equiv \boldsymbol{F}/(cE)$, where $f \equiv |\boldsymbol{f}|$ is the flux-factor, $D^{ij} \equiv P^{ij}/E$, the Eddington tensor, and $q^{ijk} \equiv Q^{ijk}/(cE)$, the normalized 3rd-moment tensor, it follows from the definition of the angular moments, Eqs. (5), that

$$|\boldsymbol{f}| \leqslant 1\,, \tag{16a}$$

$$D^{ij} \leqslant 1\,, \tag{16b}$$

$$\sum_j D^{jj} = 1\,, \tag{16c}$$

$$|q^{ijk}| \leqslant 1\,, \tag{16d}$$

$$\sum_j q^{ijj} = \sum_j q^{jij} = \sum_j q^{jji} = f^i\,, \tag{16e}$$

must hold at any time. In the "free-streaming limit", which is approached far away from regions of radiation–matter interaction, all of the radiation propagates into a single direction away from its source and it must hold

$$f = 1 \quad , \quad D^{ij} = n^i_{\boldsymbol{F}} n^j_{\boldsymbol{F}}\,, \quad , \quad q^{ijk} = n^i_{\boldsymbol{F}} n^j_{\boldsymbol{F}} n^k_{\boldsymbol{F}}\,, \tag{17}$$

with $n^i_{\boldsymbol{F}} \equiv F^i/|\boldsymbol{F}|$ denoting the direction of the flux density. In the opposite limit of very frequent interactions, i.e. in the "diffusion limit", the specific intensity is approximately isotropic. Ignoring velocity terms, the radiation moment equations degenerate in this limit to the diffusion equation

$$\partial_t E + \nabla_i \left(-\frac{c}{3\kappa_{\mathrm{tra}}} \nabla^i E \right) = C^{(0)} \tag{18}$$

and the relations

$$\boldsymbol{f} = -\frac{1}{3\kappa_{\mathrm{tra}}} \frac{\nabla E}{E} \quad , \quad D^{ij} = \frac{1}{3}\,\delta^{ij}\,. \tag{19}$$

In the following sections, we will outline the basic concepts of FLD and AEF schemes and present several closure prescriptions. In Sec. 4.3.1, we will explicitly compare both methods and the presented closures on the basis of the neutrino radiation field produced by a proto-NS.

2.4.1 Flux-limited diffusion method

The approach of FLD (e.g. Wilson et al. 1975; Levermore & Pomraning 1981) is to truncate the set of moment equations at the level of the 1st-moment equation and to derive an expression for the flux density based on the diffusion limit described by Eqs. (18) and (19). Introducing the "Knudsen number" $R = |\boldsymbol{R}|$, with

$$\boldsymbol{R} \equiv \frac{1}{\omega\,\kappa_{\mathrm{tra}}} \frac{\nabla E}{E}\,, \tag{20}$$

where

$$\omega \equiv (\kappa_{\mathrm{s}} E + \kappa_{\mathrm{a}} E^{\mathrm{eq}})/(\kappa_{\mathrm{tra}} E) \tag{21}$$

is the "effective albedo", the flux density $\boldsymbol{F}_{\mathrm{FLD}}$ is prescribed as

$$\boldsymbol{F}_{\mathrm{FLD}} = -\,\Lambda(R)\,\boldsymbol{R} cE\,, \tag{22}$$

in which $\Lambda(R)$ is called the "flux-limiter". The latter is constructed such that the flux density correctly preserves the constraints of Eqs. (17), (19). To this end the limits

$$\lim_{R\to\infty} \Lambda(R)\,R = 1, \tag{23}$$

and

$$\lim_{R\to 0} \Lambda(R) = \frac{1}{3}\,, \tag{24}$$

respectively, have to be fulfilled (note that $\omega \to 1$ in the diffusion limit). Three prescriptions are widely used in the literature (Wilson et al. 1975; Liebendörfer et al. 2004; Levermore & Pomraning 1981):

$$\Lambda_{\mathrm{Wilson}}(R) = \frac{1}{3+R}\,, \tag{25a}$$

$$\Lambda_{\mathrm{Bruenn}}(R) = \begin{cases} \min\left(\Lambda_{\mathrm{Wilson}}(R), \frac{1+\sqrt{1-(r_\nu/r)^2}}{2R}\right) & , r > r_\nu \\ \Lambda_{\mathrm{Wilson}}(R) & , \text{else}\,, \end{cases} \tag{25b}$$

$$\Lambda_{\mathrm{Levermore}}(R) = \frac{1}{R}\left(\coth R - \frac{1}{R}\right)\,. \tag{25c}$$

The limiter in Eq. (25b) is only designed for the spherically symmetric case in which r is the radius coordinate and r_ν is the radius of a (properly defined) neutrinosphere. The limitation for $r > r_\nu$ is intended to ensure that the neutrino flux cannot be higher than if the neutrinos were distributed isotropically into a finite cone subtending the sphere of radius r_ν.

The main drawbacks of FLD are: First, the prescription of the flux density is in general not consistent with the 1st-moment equation. As a direct consequence, the full RHD system suffers from momentum and therefore energy non-conservation (Bruenn 1985; Baron et al. 1989) whenever momentum transfer between matter and radiation takes place. In the case of CCSNe, the violation is found (Cernohorsky &

van den Horn 1990) to be particularly significant in the semi-transparent region where $\Lambda(R)$ undergoes the main part of the transition $1/3 \to 0$. Even though interim solutions of this shortcoming can be formulated, e.g. by introducing an artificial opacity (Janka 1991; Dgani & Janka 1992) that contains the missing information of the 1st-moment equation, they introduce further degrees of freedom, hence rendering the resulting method rather tuned to special cases.

Second, in more than one dimension a complication arises from the fact that the flux density vector is always directed opposite to the gradient of the energy density since the pressure is effectively isotropic (cf. Eq. (19)): Radiation in the free-streaming limit will not keep its original flux direction after closely passing opaque objects. Instead it behaves like a gas and fills up space in every direction, unable to form persistent shadows.

The third issue is a purely computational aspect: The energy equation evolved in FLD is – at least whenever $f \neq 1$ – of parabolic mathematical nature. As such, it comes with the property that the operator $\nabla \cdot \boldsymbol{F}$ needs to be treated time-implicitly in most practical cases. This is because the characteristic timescale $\tau_{\rm FLD}$ associated with $\nabla \cdot \boldsymbol{F}$ can become extremely short in the optically thin limit $\kappa_{\rm tra} \to 0$. One can roughly estimate the local timescale $\tau_{\rm FLD}$ by thinking of the operator $\nabla \cdot \boldsymbol{F}$ as being locally a linear convex combination of the advection operator $\alpha \boldsymbol{f} c \nabla E$ and the diffusion operator $(1-\alpha)(-\Lambda c/\kappa_{\rm tra})\nabla^2 E$, with some weighting factor $0 < \alpha < 1$. A heuristic dimensional analysis then gives

$$\frac{E}{\tau_{\rm FLD}} \sim \alpha \frac{c}{\Delta x} f E + (1-\alpha) \frac{c}{\kappa_{\rm tra} \Delta x^2} \Lambda E \tag{26a}$$

$$\Rightarrow \tau_{\rm FLD} \sim \left(\frac{\alpha f}{\tau_{\rm adv}} + \frac{(1-\alpha) 3\Lambda}{\tau_{\rm diff}} \right)^{-1} , \tag{26b}$$

where Δx is the local grid size and

$$\tau_{\rm adv} \equiv \Delta x / c \,, \tag{27a}$$

$$\tau_{\rm diff} \equiv 3 \kappa_{\rm tra} \Delta x^2 / c \tag{27b}$$

are the characteristic timescales of advection and diffusion, respectively. Hence, owing to the fact that $\tau_{\rm diff} \to 0$ in optically thin regions, $\tau_{\rm FLD}$ can drop significantly below $\tau_{\rm adv}$.

2.4.2 Algebraic Eddington factor method

In the AEF method the truncation of the moment equations takes place at the level of the 2nd-moment equation, i.e. the Eddington tensor is expressed as a function of evolved quantities. Besides resolving by construction the first two drawbacks of the FLD scheme mentioned in Sec. 2.4.1, another important computational difference to the FLD scheme is that the equations solved in the AEF scheme are intrinsically hyperbolic, which allows to use explicit time integration methods (at least for all but the source terms, see Sec. 3) with time steps not lower than the minimum of $\tau_{\rm adv}$ over the computational domain.

Historically, algebraic closures have been constructed and analyzed most often in the context of one-dimensional systems and up to the present day quite a number of one-dimensional closures have been proposed in the literature. The algebraic Eddington factor $\chi \equiv P/E$ is typically expressed as $\chi = \chi(e, f)$, where $e = (4\pi)^{-1} \int {\rm d}\Omega \mathcal{F} = (hc)^3/(4\pi\epsilon)^3 E$. Note that in constrast to the FLD scheme, the closure only depends on radiation moments and not on the opacities. In the course of this paper we consider a variety of closures, of which the Eddington factors are given by

$$\chi_{\rm Minerbo}(f) = \frac{1}{3} + \frac{1}{15} \left(6f^2 - 2f^3 + 6f^4 \right) , \tag{28a}$$

$$\chi_{M_1}(f) = \frac{3 + 4f^2}{5 + 2\sqrt{4 - 3f^2}} \,, \tag{28b}$$

$$\chi_{\rm Janka}(f) = \frac{1}{3} \left(1 + \frac{1}{2} f^{1.31} + \frac{3}{2} f^{3.56} \right) , \tag{28c}$$

$$\chi_{\rm Max.Ent.}(e, f) = \frac{2}{3}(1-e)(1-2e)\sigma\left(\frac{f}{1-e} \right) + \frac{1}{3} \,, \tag{28d}$$

where $\sigma(x) \equiv x^2(3 - x + 3x^2)/5$ in Eq. (28d). The statistical closure $\chi_{\rm Minerbo}(f)$ by Minerbo (1978) assumes a fermionic particle distribution with low density ($e \to 0$) to be in the state of maximum entropy. The generalization of this closure is $\chi_{\rm Max.Ent.}(e, f)$, derived by Cernohorsky & Bludman (1994), which additionally to $\chi_{\rm Minerbo}$ takes into account the effects of fermion blocking for $e > 0$. In Eqs. (28a), (28d) we employed the polynomial approximation derived by Cernohorsky & Bludman (1994) to circumvent the numerical inversion of the Langevin function occurring in the original formulations of both closures. The M_1 closure can either be derived from the assumption of the radiation field being isotropic in some unspecified frame of reference (Levermore 1984) or from maximizing a photon entropy functional (Dubroca & Feugeas 1999). Note that in both aforementioned derivations the M_1 closure actually relates the energy-integrated moments. In our present treatment, in contrast, we apply all closure relations in Eqs. (28) individually for each neutrino energy ϵ. Finally, the closure by Janka (1991) was obtained by fitting the neutrino radiation profile around a proto-NS calculated with Monte-Carlo methods. For further detailed discussions about specific one-dimensional closures and their properties, see, e.g., Smit et al. (2000) and Pons et al. (2000).

To extend the one-dimensional Eddington factor χ to the multidimensional Eddington tensor D^{ij} and the 3rd-moment tensor q^{ijk}, we make use of the underlying assumption that these tensors are only a function of the scalar E and the vector $\boldsymbol{F}$[6]. From symmetry arguments it follows that D^{ij} must be symmetric with respect to rotation around the flux direction, $\boldsymbol{n_F} \equiv \boldsymbol{F}/|\boldsymbol{F}|$, which is only fulfilled if D^{ij} is a linear combination of the two tensors δ^{ij} and $n^i_{\boldsymbol{F}} n^j_{\boldsymbol{F}}$ (e.g. Pennisi & Trovato 1987). After using the trace condition of Eq. (16c) the two remaining coefficients can be expressed as functions of a single parameter, χ, which is the multidimensional generalization of the Eddington factor and is defined as

$$\chi \equiv \frac{\int {\rm d}\Omega \, (\boldsymbol{n} \cdot \boldsymbol{n_F})^2 \, \mathcal{F}}{\int {\rm d}\Omega \, \mathcal{F}} \,. \tag{29}$$

The Eddington tensor then reads (e.g. Levermore 1984):

$$D^{ij} = \frac{1-\chi}{2} \, \delta^{ij} + \frac{3\chi - 1}{2} \, n^i_{\boldsymbol{F}} \, n^j_{\boldsymbol{F}} \,. \tag{30}$$

[6] Mathematically speaking, we assume D^{ij} and q^{ijk} to be *isotropic tensor functions* (e.g. Pennisi & Trovato 1987) of E and $\boldsymbol{F}$, which in particular implies that these functions may not depend on derivatives of E or $\boldsymbol{F}$.

The energy-dependent comoving-frame moment equations, Eqs. (7), also contain the 3rd moments, q^{ijk}. In analogy to the derivation of D^{ij} above, the condition that this tensor only depends on E and $\boldsymbol{F}$ must result in q^{ijk} being invariant under rotation around $\boldsymbol{n}_{\boldsymbol{F}}$, which is only fulfilled if q^{ijk} is a linear combination of $n^i_{\boldsymbol{F}}\delta^{jk}$, $n^j_{\boldsymbol{F}}\delta^{ik}$ and $n^k_{\boldsymbol{F}}\delta^{ij}$ as well as $n^i_{\boldsymbol{F}}n^j_{\boldsymbol{F}}n^k_{\boldsymbol{F}}$ (e.g. Pennisi 1992). The corresponding coefficients can be eliminated using the trace conditions of Eq. (16e) in favor of a single parameter, q, defined as

$$q \equiv \frac{\int \mathrm{d}\Omega\ (\boldsymbol{n}\cdot\boldsymbol{n}_{\boldsymbol{F}})^3\,\mathcal{F}}{\int \mathrm{d}\Omega\,\mathcal{F}}\,, \tag{31}$$

yielding for the 3rd-moment tensor:

$$q^{ijk} = \frac{f-q}{2}(n^i_{\boldsymbol{F}}\delta^{jk} + n^j_{\boldsymbol{F}}\delta^{ik} + n^k_{\boldsymbol{F}}\delta^{ij}) + \frac{5q-3f}{2}\,n^i_{\boldsymbol{F}}\,n^j_{\boldsymbol{F}}\,n^k_{\boldsymbol{F}}\,. \tag{32}$$

The 3rd-moment factor q explicitly depends on the distribution function. Therefore, only closures that dictate an explicit functional form of the distribution function are suited for the computation of the 3rd moment, unless additional assumptions are made in the construction of the closure. For the Minerbo closure, the factor q can be calculated in a straightforward manner in analogy to the derivation of χ (Minerbo 1978) and reads (again using the polynomial approximation of the Langevin function as given in Cernohorsky & Bludman 1994)

$$q_{\mathrm{Minerbo}}(f) = \frac{f}{75}(45{+}10f{-}12f^2{-}12f^3{+}38f^4{-}12f^5{+}18f^6)\,. \tag{33}$$

We outline the derivation of Eq. (33) in Appendix A. Recently, Vaytet et al. (2011) calculated the 3rd-moment factor q also for the M_1 closure.

3 NUMERICAL METHOD

3.1 Motivation of the integration scheme

Before presenting the details of the numerical implementation of the AEF scheme outlined in the previous section, we briefly summarize and motivate the general framework of the discretization scheme. Owing to the fact that the advection-type operators on the left-hand side of the two-moment system, Eqs. (7), are of hyperbolic mathematical nature, we can employ Godunov-type finite-volume methods commonly used in numerical hydrodynamics to discretize these operators. However, in regions of strong coupling with matter the source terms become stiff and the moment equations approach the parabolic diffusion limit. Hence, the time integration is performed in a mixed explicit–implicit manner, in which all terms on the left-hand side of Eqs. (7) are treated explicitly in time while the source terms on the right-hand side of Eqs. (7) are handled implicitly (at least whenever being in the stiff regime). In that way the overall time step used for integration of the whole scheme is constrained by the Courant condition to be on the order of the advection timescale $\tau_{\mathrm{adv}} \equiv \Delta x/c$, i.e. the light-crossing time of grid cells with width Δx. The alternative would be to integrate the full two-moment system implicitly in time. In that case the computational cost per time step would be significantly higher (particularly in the multidimensional case) but on the other hand this would allow to employ a larger time step which is closer to the fluid-dynamical time step $\Delta x/v$. We opted for the former version of integration, mainly for the following reasons:

(1) Since the velocities in CCSNe and NS mergers are typically rather high, $v \sim \mathcal{O}(0.1c)$, the characteristic hydrodynamics time step and therefore the implicit radiation time step turn out to be only a factor of a few greater than the explicit radiation time step. (2) Since all operators containing spatial derivatives are treated explicitly, the common parallelization methods can be applied with very high efficiency. This is particularly advantageous in the multidimensional case in which a fully implicit scheme would become increasingly expensive (as its computational cost typically increases faster than linear with the number of grid zones). (3) Light fronts and discontinuities in the radiation field can be sharply resolved, which tend to be smeared out in an implicit method, unless a time step comparable to the explicit one is used. (4) The overall numerical implementation is less involved than for an implicit scheme because inversions of large matrices that couple spatial grid points are avoided. (5) While high-order spatial reconstruction methods can be implemented in a straightforward manner in explicit schemes, they are usually too prohibitive to be used in implicit schemes.

For other implementations of a similar explicit–implicit integration method see,e.g. Sądowski et al. (2013), Skinner & Ostriker (2013), O'Connor (2014). For implementations of fully implicit schemes see, e.g., Audit et al. (2002), Hayes & Norman (2003).

3.2 Basic discretization scheme

The spatial and energy-space discretization scheme for all quantities is based on the finite-volume approach. The set of spatial coordinates can be varied between Cartesian (x, y, z), cylindrical and spherical polar (r, θ, ϕ) coordinates. However, for outlining the discretization scheme in this section we will restrict ourselves to Cartesian coordinates. The extension to curvilinear coordinates is realized by adding the appropriate geometric source terms to the presented discretized derivatives. The geometric source terms are purely algebraic functions of the evolved quantities and the grid coordinates and are discretized simply by replacing the arguments of these functions with the corresponding discretized quantities.

The spatial grid is composed of volume cells $(\mathsf{i},\mathsf{j},\mathsf{k})$ that are obtained after discretizing a given domain in each coordinate direction $\{x, y, z\}$ into $\{N_x, N_y, N_z\}$ zones, of which each is defined by the cell boundaries $x_{\mathsf{i}\pm\frac{1}{2}}, y_{\mathsf{j}\pm\frac{1}{2}}, z_{\mathsf{k}\pm\frac{1}{2}}$, with $\{\mathsf{i},\mathsf{j},\mathsf{k}\} = \{1\ldots N_x, 1\ldots N_y, 1\ldots N_z\}$. The cell-center coordinates are computed as $x_{\mathsf{i}} \equiv 1/2(x_{\mathsf{i}-\frac{1}{2}} + x_{\mathsf{i}+\frac{1}{2}})$ and analog for the other directions. The volume of cell $(\mathsf{i},\mathsf{j},\mathsf{k})$ is denoted by $\Delta V_{\mathsf{i},\mathsf{j},\mathsf{k}}$, and the area of the surface $(\mathsf{i}+\frac{1}{2},\mathsf{j},\mathsf{k})$, located between cells $(\mathsf{i},\mathsf{j},\mathsf{k})$ and $(\mathsf{i}+1,\mathsf{j},\mathsf{k})$, is denoted by $\Delta A_{\mathsf{i}+\frac{1}{2},\mathsf{j},\mathsf{k}}$.

For the grid in energy space, given by N_ϵ energy bins, we use $\epsilon_{\xi\pm\frac{1}{2}}$ to denote the boundaries of the ξ'th bin, with $\xi = 1\ldots N_\epsilon$. Furthermore, $\epsilon_\xi \equiv 1/2(\epsilon_{\xi+\frac{1}{2}} + \epsilon_{\xi-\frac{1}{2}})$ and $\Delta\epsilon_\xi \equiv \epsilon_{\xi+\frac{1}{2}} - \epsilon_{\xi-\frac{1}{2}}$ define the center and width of the ξ'th bin, respectively.

We define the radiation fields as well as the fluid quantities on the same spatial grid. The discrete representa-

tions $\hat{U} \in \{\hat{\rho}, (\hat{\rho Y_e}), (\hat{\rho v^i}), \hat{e}_\mathrm{t}\}$ of the hydrodynamic quantities $U \in \{\rho, \rho Y_e, \rho v^i, e_\mathrm{t}\}$ are interpreted as cell-volume averages in space, i.e. as

$$\hat{U}_{\mathsf{i},\mathsf{j},\mathsf{k}} \equiv \frac{1}{\Delta V_{\mathsf{i},\mathsf{j},\mathsf{k}}} \int_{\Delta V_{\mathsf{i},\mathsf{j},\mathsf{k}}} \mathrm{d}V\, U\,, \tag{34}$$

while the discrete representations $\hat{X} \in \{\hat{E}, \hat{F}^i, \hat{P}^{ij}, \hat{Q}^{ijk}\}$ of the radiation moments $X \in \{E, F^i, P^{ij}, Q^{ijk}\}$ are interpreted as averages in space and integrals in energy space in the following way

$$\hat{X}_{\mathsf{i},\mathsf{j},\mathsf{k},\xi} \equiv \frac{1}{\Delta V_{\mathsf{i},\mathsf{j},\mathsf{k}}} \int_{\Delta V_{\mathsf{i},\mathsf{j},\mathsf{k}}} \mathrm{d}V \int_{\Delta\epsilon_\xi} \mathrm{d}\epsilon\, X\,. \tag{35}$$

The spatial and energy discretization of the moment equations, Eqs (7), is realized by applying the spatial averaging and the energy integration as in Eq. (35) to the moment equations.

The discretization of the spatial derivatives demands it to reconstruct quantities from cell-volume averages to cell-face averages, which for example on the cell-face $(\mathsf{i}+\frac{1}{2},\mathsf{j},\mathsf{k})$ are given by

$$\hat{X}_{\mathsf{i}+\frac{1}{2},\mathsf{j},\mathsf{k},\xi} \equiv \frac{1}{\Delta A_{\mathsf{i}+\frac{1}{2},\mathsf{j},\mathsf{k}}} \int_{\Delta A_{\mathsf{i}+\frac{1}{2},\mathsf{j},\mathsf{k}}} \mathrm{d}A \int_{\Delta\epsilon_\xi} \mathrm{d}\epsilon X\,. \tag{36}$$

The reconstruction algorithms that we use are adopted from the hydrodynamics part of the code and can be switched between piecewise-constant, piecewise-linear and high-order "monotonicity preserving" (MP) schemes (Suresh & Huynh 1997) or "weighted essentially non-oscillatory" (WENO) schemes (Liu et al. 1994). In what follows, we symbolically use $\hat{X}^\mathrm{L}$ and $\hat{X}^\mathrm{R}$ to denote the reconstructed values of a quantity $\hat{X}$ on the left- and right-hand side of an interface, respectively.

3.3 Summary of the integration algorithm

In order to formulate the algorithm to integrate the evolution equations for the radiation moments, $\mathbf{X} \equiv (E, \boldsymbol{F})$ (cf. Eqs. (7)), and for the fluid quantities, $\mathbf{U} \equiv (\rho, \rho Y_e, \rho\boldsymbol{v}, e_\mathrm{t})$ (cf. Eqs. (12)), we decompose these equations in the following way:

$$\partial_t \mathbf{X} + (\delta_t \mathbf{X})_\mathrm{hyp} + (\delta_t \mathbf{X})_\mathrm{vel} = (\delta_t \mathbf{X})_\mathrm{src}\,, \tag{37a}$$

$$\partial_t \mathbf{U} + (\delta_t \mathbf{U})_\mathrm{hyd} = (\delta_t \mathbf{U})_\mathrm{src}\,. \tag{37b}$$

In Eq. (37a), $(\delta_t \mathbf{X})_\mathrm{hyp} \equiv \left(\nabla_j F^j, c^2 \nabla_j P^{ij}\right)$ represents the velocity-independent hyperbolic advection terms, while all velocity-dependent terms are subsumed in $(\delta_t \mathbf{X})_\mathrm{vel}$, and the interaction source terms are represented by $(\delta_t \mathbf{X})_\mathrm{src}$. In Eq. (37b), $(\delta_t \mathbf{U})_\mathrm{src}$ are the radiative source terms given by Eqs. (13), while all remaining terms representing non-radiative physics are contained in $(\delta_t \mathbf{U})_\mathrm{hyd}$. We first summarize the overall integration scheme of Eqs. (37). Subsequently, in Secs. 3.4–3.7 we will explicitly describe how the individual terms are computed.

The following steps are performed to evolve the RHD equations, Eqs. (37), from time t^n to $t^{\mathsf{n}+1} = t^\mathsf{n} + \Delta t$. Note that we use the shorthand notation $\hat{A}^\mathsf{n} \equiv \hat{A}(t^\mathsf{n})$ to refer to a quantity $\hat{A}$ at some time step t^n:

1) Compute the global integration time step Δt used for both hydrodynamics and radiation transport as ($i \in \{x, y, z\}$):

$$\Delta t_\mathrm{rad} = \min_{\mathsf{i},\mathsf{j},\mathsf{k},i} \left\{ \frac{(\Delta x)^i_{\mathsf{i},\mathsf{j},\mathsf{k}}}{|v^i_{\mathsf{i},\mathsf{j},\mathsf{k}}| + \max|(\lambda_\pm)^i_{\mathsf{i},\mathsf{j},\mathsf{k}}|} \right\}, \tag{38a}$$

$$\Delta t_\mathrm{hyd} = \min_{\mathsf{i},\mathsf{j},\mathsf{k},i} \left\{ \frac{(\Delta x)^i_{\mathsf{i},\mathsf{j},\mathsf{k}}}{\max|(\lambda_\mathrm{fluid})^i_{\mathsf{i},\mathsf{j},\mathsf{k}}|} \right\}, \tag{38b}$$

$$\Delta t = \mathrm{CFL} \cdot \min\left\{\Delta t_\mathrm{rad}, \Delta t_\mathrm{hyd}\right\}, \tag{38c}$$

where $\lambda_\pm$ and λ_fluid are the characteristic velocities of the radiation system (cf. Eqs. (46, 47)) and of the fluid, respectively, CFL is the chosen Courant-Friedrichs-Lewy number and $(\Delta x)^i_{\mathsf{i},\mathsf{j},\mathsf{k}}$ is the length of cell $(\mathsf{i},\mathsf{j},\mathsf{k})$ in coordinate direction i.

2) Construct the advection operator $(\delta_t \hat{\mathbf{X}})^\mathsf{n}_\mathrm{adv} \equiv (\delta_t \hat{\mathbf{X}})^\mathsf{n}_\mathrm{hyp} + (\delta_t \hat{\mathbf{X}})^\mathsf{n}_\mathrm{vel}$ as a function of the radiation moments $\hat{\mathbf{X}}^\mathsf{n}$ and fluid quantities $\hat{\mathbf{U}}^\mathsf{n}$ using the discretization rules described in Secs. 3.4 and 3.5.

3) Compute the hydrodynamics evolution operator $(\delta_t \hat{\mathbf{U}})^\mathsf{n}_\mathrm{hyd}$ as a function of $\hat{\mathbf{U}}^\mathsf{n}$. Eventually, add other properly discretized terms to $(\delta_t \hat{\mathbf{U}})^\mathsf{n}_\mathrm{hyd}$ corresponding to additional, non-radiative physics (such as gravitation or magnetic fields).

4) Perform an intermediate update to the time $t^{\mathsf{n}+\frac{1}{2}} \equiv t^\mathsf{n} + \Delta t/2$ by solving

$$\hat{\mathbf{X}}^{\mathsf{n}+\frac{1}{2}} = \hat{\mathbf{X}}^\mathsf{n} + \frac{\Delta t}{2}\left[-(\delta_t \hat{\mathbf{X}})^\mathsf{n}_\mathrm{adv} + (\delta_t \hat{\mathbf{X}})^{\mathsf{n},\mathsf{n}+\frac{1}{2}}_\mathrm{src}\right], \tag{39a}$$

$$\hat{\mathbf{U}}^{\mathsf{n}+\frac{1}{2}} = \hat{\mathbf{U}}^\mathsf{n} + \frac{\Delta t}{2}\left[-(\delta_t \hat{\mathbf{U}})^\mathsf{n}_\mathrm{hyd} + (\delta_t \hat{\mathbf{U}})^{\mathsf{n},\mathsf{n}+\frac{1}{2}}_\mathrm{src}\right] \tag{39b}$$

for $\hat{\mathbf{X}}^{\mathsf{n}+\frac{1}{2}}$, $\hat{\mathbf{U}}^{\mathsf{n}+\frac{1}{2}}$, where the two comma-separated superscripts indicate that the source terms can generally depend on the hydro- and radiation variables at both the old and the new time step, accounting for the fact that the integration can be performed explicitly and/or implicitly as the circumstances require (cf. Sec. 3.6).

5) In analogy to steps *2)* and *3)* use $\hat{\mathbf{X}}^{\mathsf{n}+\frac{1}{2}}$ and $\hat{\mathbf{U}}^{\mathsf{n}+\frac{1}{2}}$ to compute $(\delta_t \hat{\mathbf{X}})^{\mathsf{n}+\frac{1}{2}}_\mathrm{adv}$ and $(\delta_t \hat{\mathbf{U}})^{\mathsf{n}+\frac{1}{2}}_\mathrm{hyd}$, respectively.

6) The quantities at $t^{\mathsf{n}+1}$ are finally obtained by solving

$$\hat{\mathbf{X}}^{\mathsf{n}+1} = \hat{\mathbf{X}}^\mathsf{n} + \Delta t\left[-(\delta_t \hat{\mathbf{X}})^{\mathsf{n}+\frac{1}{2}}_\mathrm{adv} + (\delta_t \hat{\mathbf{X}})^{\mathsf{n}+\frac{1}{2},\mathsf{n}+1}_\mathrm{src}\right], \tag{40a}$$

$$\hat{\mathbf{U}}^{\mathsf{n}+1} = \hat{\mathbf{U}}^\mathsf{n} + \Delta t\left[-(\delta_t \hat{\mathbf{U}})^{\mathsf{n}+\frac{1}{2}}_\mathrm{hyd} + (\delta_t \hat{\mathbf{U}})^{\mathsf{n}+\frac{1}{2},\mathsf{n}+1}_\mathrm{src}\right] \tag{40b}$$

for $\hat{\mathbf{X}}^{\mathsf{n}+1}$, $\hat{\mathbf{U}}^{\mathsf{n}+1}$ in an analog manner as in step *4)*.

The above update scheme is formally unsplit[7] and is 2nd-order accurate in time with respect to all explicit (advection or source) terms and 1st-order accurate with respect to implicit source terms. Although realizations of higher-order implicit–explicit (IMEX) schemes exist (e.g. Ascher et al. 1997; Pareschi & Russo 2005; McKinney et al. 2014) we

[7] By *unsplit*, we refer to the property that the advection and source terms are integrated within a single step, in contrast to which in a *split* scheme the quantities would be updated first for one set of terms (including the recomputation of primitive variables such as temperatures, opacities and Eddington factors) before calculating the other set of terms.

found that the method described above is sufficiently robust and accurate in all applications we considered so far.

3.4 Velocity-independent hyperbolic part

Our basic treatment of the velocity-independent, hyperbolic part of the two-moment system, Eqs. (7), follows along the lines of Pons et al. (2000) and Audit et al. (2002). The notion is to exploit a Godunov method (Godunov 1959) as the basis for a high-resolution shock capturing scheme that solves the local Riemann problems between discontinuous states at the interfaces of grid cells. We start the presentation of its working method by considering the one-dimensional system

$$\partial_t \begin{pmatrix} E \\ F \end{pmatrix} + \partial_x \begin{pmatrix} F \\ c^2\chi E \end{pmatrix} = 0\,, \tag{41}$$

where the algebraic closure $\chi = \chi(e,f)$ is a function of e and f. This system is hyperbolic if the Jacobian matrix $\mathcal{J}$ of the vector of fluxes $(F, c^2\chi E)^{\mathrm{T}}$,

$$\mathcal{J} = \begin{pmatrix} 0 & 1 \\ c^2(\chi + e\frac{\partial\chi}{\partial e} - f\frac{\partial\chi}{\partial f}) & c\frac{\partial\chi}{\partial f} \end{pmatrix}, \tag{42}$$

has real eigenvalues $\lambda_\pm^{\mathrm{1D}}$, given by

$$\lambda_\pm^{\mathrm{1D}} = \frac{c}{2}\frac{\partial\chi}{\partial f} \pm \frac{c}{2}\sqrt{\frac{\partial\chi}{\partial f}^2 + 4(\chi + e\frac{\partial\chi}{\partial e} - f\frac{\partial\chi}{\partial f})}\,. \tag{43}$$

All of the closures listed in Eqs. (28) fulfill the condition of hyperbolicity and lead to the following properties: In the free-streaming limit, $f \to 1$, we have

$$\chi = 1\ ,\ \lambda_+^{\mathrm{1D}} = +c\ ,\ \lambda_-^{\mathrm{1D}} = (\frac{\partial\chi}{\partial f} - 1)c\,, \tag{44}$$

while in the diffusion limit, $f \to 0$, one obtains

$$\chi = \frac{1}{3} \quad , \quad \lambda_\pm^{\mathrm{1D}} = \pm\frac{1}{\sqrt{3}}c\,. \tag{45}$$

That is, the limiting cases for the Eddington factor and the wave speeds are consistent with what is dictated by the Boltzmann equation.

In the multidimensional generalization of Eq. (41) the matrix eigenvalues contain an additional dependence on the direction cosine $\mu \equiv \cos\alpha_{\boldsymbol{F}}$, where $\alpha_{\boldsymbol{F}}$ is the angle between the direction of the radiation flux vector $\boldsymbol{F}$ and the coordinate direction with respect to which the derivative is taken. The wave speeds are now obtained as roots of a cubic polynomial leading, at least in terms of a general closure, to rather large expressions[8]. For practical purposes we do not take into account the exact angular dependence of the eigenvalues[9] $\lambda_\pm^{\mathrm{exact}}(\mu)$ but we instead approximate the latter using the following 1st-order expansion in μ:

$$\lambda_\pm(\mu) = \lambda_\pm^{\mathrm{exact}}(0) + |\mu|\left(\lambda_\pm^{\mathrm{exact}}(1) - \lambda_\pm^{\mathrm{exact}}(0)\right)\,, \tag{46}$$

where

$$\lambda_\pm^{\mathrm{exact}}(1) = \lambda_\pm^{\mathrm{1D}}\,, \tag{47a}$$

$$\lambda_\pm^{\mathrm{exact}}(0) = \pm\frac{c}{2}\sqrt{2(1-\chi-e\frac{\partial\chi}{\partial e}) + \frac{1}{f}\frac{\partial\chi}{\partial f}(1+2f^2-3\chi)}\,. \tag{47b}$$

In Appendix B we provide the components of the Jacobian in terms of a general closure $\chi(e,f)$ and show plots of the exact and linearized wave speeds for some specific closures. These plots indicate that the linearized wave speeds reproduce the exact wave speeds sufficiently well for the former to be used instead of the latter as estimates for signal speeds of an approximate Riemann solver (see below). It is worth to note that the qualitative behavior of the angular dependence of the wave speeds, $\lambda_\pm$, is physically consistent with the underlying Boltzmann equation: In the diffusion regime, $f \ll 1$, the wave speeds become nearly isotropic with $|\lambda_\pm| \to c/\sqrt{3}$, while in the free-streaming regime, $f \to 1$, the wave speeds become forward-peaked with $\lambda_\pm \to c$ in the direction of $\boldsymbol{F}$ and $\lambda_\pm \to 0$ orthogonally to $\boldsymbol{F}$.

In a fashion that is commonly employed in numerical hydrodynamics, we use the above velocities as signal speeds for an approximate Riemann solver in order to compute the numerical fluxes through each cell interface. We use the two-wave solver by Harten, Lax and van Leer (HLL, Harten et al. 1983), which approximates the final numerical interface fluxes as functions of the left-/right-hand side fluxes $\mathsf{F}^{\mathrm{L/R}}$ (with $\mathsf{F} \in \{F^i, c^2P^{ij}\}$) and states $\mathsf{U}^{\mathrm{L/R}}$ (with $\mathsf{U} \in \{E, F^i\}$) as

$$\mathsf{F}^{\mathrm{HLL}} \equiv \frac{\lambda_+^{\mathrm{HLL}}\mathsf{F}^{\mathrm{L}} - \lambda_-^{\mathrm{HLL}}\mathsf{F}^{\mathrm{R}}}{\lambda_+^{\mathrm{HLL}} - \lambda_-^{\mathrm{HLL}}} + \frac{\lambda_+^{\mathrm{HLL}}\lambda_-^{\mathrm{HLL}}\left(\mathsf{U}^{\mathrm{R}} - \mathsf{U}^{\mathrm{L}}\right)}{\lambda_+^{\mathrm{HLL}} - \lambda_-^{\mathrm{HLL}}}\,, \tag{48}$$

with the signal speeds $\lambda_+^{\mathrm{HLL}} = \max(0, \lambda_+^{\mathrm{L}}, \lambda_+^{\mathrm{R}})$ and $\lambda_-^{\mathrm{HLL}} = \min(0, \lambda_-^{\mathrm{L}}, \lambda_-^{\mathrm{R}})$. All quantities labeled by L/R in this flux formula are computed using the cell-interface reconstructed moments $\hat{E}^{\mathrm{L/R}}, \hat{F}^{i,\mathrm{L/R}}$. Applying this solver, the final spatially-discretized version of the operator $(\delta_t X)_{\mathrm{hyp}}$ of Eq. (37a) reads (using $\hat{X} \in \{\hat{E}, \hat{F}\}$)

$$\left(\delta_t \hat{X}_{\mathsf{i,j,k},\xi}\right)_{\mathrm{hyp}} = \frac{\Delta A_{\mathsf{i}+\frac{1}{2},\mathsf{j},\mathsf{k}}\mathsf{F}^{\mathrm{HLL}}_{\mathsf{i}+\frac{1}{2},\mathsf{j},\mathsf{k},\xi} - \Delta A_{\mathsf{i}-\frac{1}{2},\mathsf{j},\mathsf{k}}\mathsf{F}^{\mathrm{HLL}}_{\mathsf{i}-\frac{1}{2},\mathsf{j},\mathsf{k},\xi}}{\Delta V_{\mathsf{i,j,k}}} + \text{“}y\text{”} + \text{“}z\text{”}\,, \tag{49}$$

where we symbolically indicated the contributions from the y- and z-directions, which are obtained in an analog manner.

Yet, there is a caveat we have to face when approaching the parabolic diffusion limit (cf. Eq. (19)) with the scheme described above, since the latter is originally designed only for hyperbolic systems. In contrast to the hyperbolic system, the parabolic diffusion equation is not associated with characteristic waves propagating information between cells with finite speeds. Hence, the ansatz of using a Riemann solver that tracks characteristics via upwinding and captures shocks by adding diffusivity is no longer justified in the parabolic diffusion regime. Instead, the fluxes in the diffusion regime should be of central type (i.e. symmetric with respect to the cell interface) and they should lead to as little as possible numerical diffusivity in order not to spoil the effects of the physical diffusivity. To handle this issue, we employ a simple switch between the two types of fluxes ac-

[8] See, however, Skinner & Ostriker (2013) who found for the particular case of the M_1 closure comparably compact expressions for the wave speeds as functions of μ and f.

[9] Note that also a third eigenvalue λ_0 appears in the multidimensional case which fulfills $\lambda_- < \lambda_0 < \lambda_+$. However, this eigenvalue is not relevant for our present purpose.

cording to:

$$\mathsf{F}^{\mathrm{HLL},*}_{\mathsf{i}+\frac{1}{2}} = \begin{cases} \mathsf{F}^{\mathrm{HLL}}_{\mathsf{i}+\frac{1}{2}} & \text{if } \mathcal{P}_{\mathsf{i}+\frac{1}{2}} < 1\,, \\ \frac{1}{2}\left(\mathsf{F}^{\mathrm{L}}_{\mathsf{i}+\frac{1}{2}} + \mathsf{F}^{\mathrm{R}}_{\mathsf{i}+\frac{1}{2}}\right) & \text{if } \mathcal{P}_{\mathsf{i}+\frac{1}{2}} > 1\,, \end{cases} \tag{50}$$

where the index "i" denotes a representative grid index for any coordinate direction and the "stiffness parameter"

$$\mathcal{P} \equiv \kappa_{\mathrm{tra}}\Delta x = \frac{\Delta x}{\lambda_\nu}\,, \tag{51}$$

is a measure of the degree of neutrino–matter coupling relative to numerically resolved scales of length and time: For $\mathcal{P} \gtrsim 1$ neutrino interactions proceed on spatial and temporal scales smaller than the grid scale Δx and shorter than the numerical time step $\Delta x/c$, respectively. Hence, for $\mathcal{P}$ exceeding unity the source terms become stiff and thereby cause the two-moment system to undergo the transition from a hyperbolic to a parabolic system. Our experience from several tests (cf. Sec. 4, particularly Sec. 4.2.2) has shown that the seemingly discontinuous jump between both flux formulations in Eq. (50) has no significant influence on the solution. This is because at the point of transition, $\mathcal{P} = 1$, one often has the situation that (1) the flux factors f are sufficiently small to lead to nearly equal contributions of F^{L} and F^{R} in $\mathsf{F}^{\mathrm{HLL}}$, and (2) the relative importance of the diffusive part of $\mathsf{F}^{\mathrm{HLL}}$ (i.e. the second term in Eq. (48)) is still negligible, particularly when using high-order spatial reconstruction.

3.5 Velocity-dependent terms

In the following we present the recipes used to discretize the velocity-dependent terms $(\delta_t X)_{\mathrm{vel}}$. In order to discretize the terms containing velocity derivatives, we reconstruct the velocities to obtain $\hat{v}^{i,\mathrm{L/R}}$ located at each cell interface by using the same reconstruction algorithm as for the radiation moments.

3.5.1 Fluid-advection terms

As fluid-advection terms we denote the (I)-terms in Eqs. (7). For their discretization we also employ an HLL-type Riemann solver for each coordinate direction analog to Eqs. (48) and (49). Specifically, we first compute fluxes $\mathsf{F}^{\mathrm{HLL,adv}}$ defined by the right-hand side of Eq. (48), but with the numerical interface fluxes $\mathsf{F}^{\mathrm{L/R}} = \hat{v}^{\mathrm{L/R}}\hat{X}^{\mathrm{L/R}}$ and the signal velocities $\lambda_+^{\mathrm{HLL}} = \max(0, \hat{v}^{\mathrm{L}}, \hat{v}^{\mathrm{R}})$ and $\lambda_-^{\mathrm{HLL}} = \min(0, \hat{v}^{\mathrm{L}}, \hat{v}^{\mathrm{R}})$, where the $\hat{v}^{\mathrm{L/R}}$ are the reconstructed velocity components normal to the interface at which the corresponding numerical flux is computed, and $\hat{X}^{\mathrm{L/R}} \in \{\hat{E}^{\mathrm{L/R}}, \hat{F}^{i,\mathrm{L/R}}\}$ are the reconstructed moments defined at the same interface. The final fluid-advection terms are then discretized exemplarily in x-direction as

$$\left(\delta_t \hat{X}_{\mathsf{i},\mathsf{j},\mathsf{k},\xi}\right)_{\mathrm{adv}} = \frac{\Delta A_{\mathsf{i}+\frac{1}{2},\mathsf{j},\mathsf{k}}\mathsf{F}^{\mathrm{HLL,adv}}_{\mathsf{i}+\frac{1}{2},\mathsf{j},\mathsf{k},\xi} - \Delta A_{\mathsf{i}-\frac{1}{2},\mathsf{j},\mathsf{k}}\mathsf{F}^{\mathrm{HLL,adv}}_{\mathsf{i}-\frac{1}{2},\mathsf{j},\mathsf{k},\xi}}{\Delta V_{\mathsf{i},\mathsf{j},\mathsf{k}}} \tag{52}$$

and analogously in the other coordinate directions.

3.5.2 Velocity derivatives

The remaining velocity derivatives are discretized exemplarily in x-direction as

$$\partial_x v^i \longrightarrow \frac{\Delta A_{\mathsf{i}+\frac{1}{2},\mathsf{j},\mathsf{k}}\hat{v}^i_{\mathsf{i}+\frac{1}{2},\mathsf{j},\mathsf{k}} - \Delta A_{\mathsf{i}-\frac{1}{2},\mathsf{j},\mathsf{k}}\hat{v}^i_{\mathsf{i}-\frac{1}{2},\mathsf{j},\mathsf{k}}}{\Delta V_{\mathsf{i},\mathsf{j},\mathsf{k}}}\,, \tag{53}$$

while to obtain unique interface velocities $\hat{v}^i_{\mathsf{i}+\frac{1}{2},\mathsf{j},\mathsf{k}}$ we arithmetically average the reconstructed velocities:

$$\hat{v}^i_{\mathsf{i}+\frac{1}{2},\mathsf{j},\mathsf{k}} = \frac{1}{2}\left(\hat{v}^{i,\mathrm{L}}_{\mathsf{i}+\frac{1}{2},\mathsf{j},\mathsf{k}} + \hat{v}^{i,\mathrm{R}}_{\mathsf{i}+\frac{1}{2},\mathsf{j},\mathsf{k}}\right)\,. \tag{54}$$

The discretization of the remaining components of $\partial_j v^i$ is given by analog expressions.

3.5.3 Doppler shift terms

In our multi-group treatment of comoving-frame radiation transport, we allow radiation energy to be redistributed between energy groups via the (IV)-terms in Eqs. (7) describing Doppler shift. From the computational point of view an important property of the Doppler shift terms is that they have a different functional structure in the energy-based moment equations, Eqs. (7), than in the number-based moment equations, Eqs. (9), albeit being physically equivalent. As a consequence, a naive discretization of the Doppler terms in the energy equation will generally lead to non-conservation of neutrino number and therefore of lepton number. Although the non-conservation could be avoided by solving the number-based moment equations in addition to the energy-based versions (e.g. Rampp & Janka 2002), this would at least double the computational expense. We therefore implemented the number-conservative method developed by Müller et al. (2010). For a detailed description of this scheme we refer the reader to the original paper; in the following we only briefly summarize the key features.

Suppressing spatial grid and tensor indices, we write the combined Doppler shift terms of the 0th-moment equation for the ξ'th energy bin as

$$\begin{aligned}\left(\delta_t \hat{E}_\xi\right)_{\mathrm{Doppler}} &= w\int_{\Delta\epsilon_\xi}\left(P - \frac{\partial \epsilon P}{\partial \epsilon}\right)\mathrm{d}\epsilon \\ &= w\left(\hat{P}_\xi + \mathbb{F}_{\xi-\frac{1}{2}} - \mathbb{F}_{\xi+\frac{1}{2}}\right)\,,\end{aligned} \tag{55}$$

where w subsumes the discretized velocity derivatives, $\hat{P}_\xi$ denotes a discretized component of the 2nd-moment tensor obtained by applying the closure relation to the discretized moments $\hat{E}_\xi$ and $\hat{F}_\xi$, and $\mathbb{F}_{\xi\pm\frac{1}{2}}$ are the discretized versions of the effective fluxes ϵP located at the energy-bin interfaces $\epsilon_{\xi\pm\frac{1}{2}}$. With the constraint that the energy-integrated number density shall be conserved, i.e. that

$$\sum_\xi \epsilon_\xi^{-1}\left(\delta_t \hat{E}_\xi\right)_{\mathrm{Doppler}} \stackrel{!}{=} 0\,, \tag{56}$$

the interface fluxes $\mathbb{F}_{\xi\pm\frac{1}{2}}$ can be written as[10]

$$\mathbb{F}_{\xi+\frac{1}{2}} = \mathbb{F}^{\mathrm{L}}_\xi + \mathbb{F}^{\mathrm{R}}_{\xi+1}\,, \tag{57}$$

[10] Note that these interface fluxes are not uniquely determined but chosen as a specific set fulfilling the imposed constraint of total number conservation.

with

$$\mathbb{F}^{\mathrm{L}}_{\xi} = \frac{1}{1-\epsilon_{\xi}\epsilon^{-1}_{\xi+1}}\hat{P}_{\xi}\gamma_{\xi} \quad , \quad \mathbb{F}^{\mathrm{R}}_{\xi} = \frac{1}{\epsilon_{\xi}\epsilon^{-1}_{\xi-1}-1}\hat{P}_{\xi}(1-\gamma_{\xi})\,. \tag{58}$$

The weighting factor $\gamma_{\xi} \in [0,1]$ can be chosen manually and we fix it similarly as in Müller et al. (2010). At the lower boundary in energy space we usually have the minimum energy $\epsilon_{1-\frac{1}{2}} = 0$ and therefore $\mathbb{F}_{1-\frac{1}{2}} = 0$. For the upper boundary at $\epsilon_{N_{\xi}+\frac{1}{2}}$ we either use an exponentially extrapolated energy distribution for the high-energy tail or the condition that the numerical flux vanishes. For the energy derivative of the 3rd moments occurring in the 1st-moment equation, Eq. (7b), we use an analog prescription as the one given above for the 2nd moments. Specifically, the Doppler shift terms for one component $\hat{F}_{\xi}$ of the 1st-moment vector (again suppressing tensor indices) is discretized as

$$\begin{aligned}\left(\delta_t \hat{F}_{\xi}\right)_{\mathrm{Doppler}} &= w\int_{\Delta\epsilon_{\xi}}\left(-\frac{\partial \epsilon Q}{\partial \epsilon}\right)\mathrm{d}\epsilon \\ &= w\left(\mathbb{F}_{\xi-\frac{1}{2}} - \mathbb{F}_{\xi+\frac{1}{2}}\right), \end{aligned} \tag{59}$$

where w again represents velocity derivatives and $\mathbb{F}_{\xi-\frac{1}{2}}$ are calculated via Eqs. (57) and (58) exactly as explained above but with $\hat{P}_{\xi}$ replaced by $\hat{Q}_{\xi}$.

3.6 Interaction source terms

As already mentioned before we intend to use a time step Δt that is close to the radiative advection timescale $\tau_{\mathrm{adv}} \equiv \Delta x/c$ to integrate the full system of moment equations. However, the numerical integration of the interaction source terms $(\delta_t X)_{\mathrm{src}}$, Eq. (37a), deserves special care because the characteristic neutrino-interaction timescale,

$$\tau_{\mathrm{int}} \equiv (c\kappa_{\mathrm{tra}})^{-1} = \lambda_{\nu}/c\,, \tag{60}$$

can become shorter than τ_{adv} by up to many orders of magnitude. In this case, i.e. for stiffness parameters $\mathcal{P} > 1$ (cf. Eq. (51)), the moment equations are stiff and a fully explicit time integration would lead to numerical instability. Hence, the source terms make an implicit treatment indispensable. However, it is important to note that the characteristic timescales of the advection-type terms $(\delta_t X)_{\mathrm{hyp}}$ and $(\delta_t X)_{\mathrm{vel}}$ (cf. Eq. (37a)) are longer than τ_{adv} also for $\mathcal{P} > 1$: In the diffusion limit the characteristic timescale of $(\delta_t X)_{\mathrm{hyp}}$ is the diffusion timescale $\tau_{\mathrm{diff}} \equiv 3\kappa_{\mathrm{tra}}\Delta x^2/c = 3\,\mathcal{P}\cdot\tau_{\mathrm{adv}} > \tau_{\mathrm{adv}}$, while the characteristic timescale of $(\delta_t X)_{\mathrm{vel}}$ is independent of the stiffness parameter and roughly approximated by[11] $\sim \Delta x/v$. Hence, we can safely apply a scheme in which the operators $(\delta_t X)_{\mathrm{hyp}}$ and $(\delta_t X)_{\mathrm{vel}}$ are treated explicitly, while the local contributions from the interaction source terms are integrated implicitly in time. Compared to an implicit treatment of the full system, this mixed-type integration greatly reduces the size of the matrix that needs to be inverted since all spatial derivatives that couple neighbouring cells on the spatial grid are handled by the explicit part.

Depending on the included types of interactions, the source terms $(\delta_t\hat{\mathbf{X}})_{\mathrm{src}}$ and $(\delta_t\hat{\mathbf{U}})_{\mathrm{src}}$ can in general each depend on all evolved radiation and hydrodynamic quantities. However, (standard) neutrino interactions do not change the baryonic mass density ρ, and they only have a marginal impact on the fluid momenta $\rho\boldsymbol{v}$, at least in typical situations where neutrino transport is relevant; hence these quantities may be treated explicitly in time. Still, if we were to integrate all but the aforementioned quantities implicitly – which means expressing the source terms $(\delta_t\hat{\mathbf{X}})_{\mathrm{src}}, (\delta_t\hat{\mathbf{U}})_{\mathrm{src}}$ as functions of these variables defined at the new time step in Eqs. (39) and (40) – we would generally need to solve a non-linear system of equations of rank $(N_{\mathrm{dim}}+1)\times N_{\epsilon}\times N_{\mathrm{spe}}+2$ (recalling that N_{dim} and N_{spe} are the number of evolved 1st-moment components and neutrino species, respecively, and N_{ϵ} is the number of energy bins), in which all radiation moments $E, \boldsymbol{F}$ as well as the gas-energy density e_{i} and the electron-number density $n_e \equiv \rho Y_e/m_{\mathrm{B}}$ are handled implicitly. However, an implicit treatment of all of these quantities is not always necessary. That is, under certain conditions a significant reduction of computational expense can be achieved by treating a subset of variables explicitly, i.e. by using the quantities defined at the old time step in the update formulae, Eqs. (39) and (40). Below we list the different modes of the source-term treatment, which we implemented in order to avoid a fully implicit integration whenever this appears justified:

a) All radiation moments $\hat{E}, \hat{\boldsymbol{F}}$ plus the hydrodynamic variables $\hat{e}_{\mathrm{i}}, \hat{n}_e$ appearing in the source terms $(\delta_t\hat{\mathbf{X}})_{\mathrm{src}}$ and $(\delta_t\hat{\mathbf{U}})_{\mathrm{src}}$ are defined at $t^{\mathrm{n}+1}$, i.e. the systems of Eqs. (39) and (40) are solved fully implicitly. Consistently, also most of the primitive variables (temperature, opacities etc.) are handled implicitly. Only the normalized 2nd- and 3rd-radiation moments χ and q (cf. Sec. 2.4.2), respectively, and the Legendre-coefficient matrices for reactions coupling multiple energy bins (see, e.g., Rampp & Janka 2002) are taken from the old time step.

b) Like *a)*, but the gas-energy density $\hat{e}_{\mathrm{i}}$ and electron-number density $\hat{n}_e$ are taken from the old time step. This reduces not only the dimensionality of the coupled non-linear system by 2, but also alleviates the computational expense by the demands of re-computing the temperatures and opacities within each iteration step of the root finding procedure.

c) Like *b)*, but all energy-coupling interactions (e.g. neutrino–electron scattering) are treated explicitly in time. The remaining source terms corresponding to emission/absorption and isoenergetic scattering can then be written as in Eqs. (14), which results in the source terms to completely decouple from each other, allowing for a straightforward implicit integration without any matrix inversion.

Since the criteria for selecting a certain integration mode are highly problem dependent, we do not specify them here; see, e.g., Sec. 4.3.2 for a particular choice in the CCSN context. In any case where a *coupled* non-linear system of equations has to be solved, we make use of the routine

[11] This estimate disregards fluxes in energy space mediated by the Doppler shift terms (see Sec. 3.5.3), which in principle can cause these terms to change on timescales shorter than $\Delta x/v$. In practice, however, these timescales are usually longer than τ_{adv} such that an explicit integration of the Doppler terms with time step $\sim \tau_{\mathrm{adv}}$ turns out to be unproblematic.

nag_nlin_sys_sol from the NAG library[12], which employs the "Broyden method" for root finding.

Based on our experience (see, e.g., last paragraph in Sec. 4.3.2) and in agreement with O'Connor (2014), the use of integration mode *a)* (i.e. an implicit treatment of $\hat{e}_{\rm i}$ and $\hat{n}_e$) is barely necessary in practice, even in regions of very high stiffness parameters, $\mathcal{P} \gg 1$. This is because in most situations where $\mathcal{P} \gg 1$ neutrinos are trapped in the gas and very close to weak equilibrium, which means that the net (absorption minus emission) source terms for $\hat{e}_{\rm i}$ and $\hat{n}_e$ are effectively small. Consequently, under these conditions $\hat{e}_{\rm i}$ and $\hat{n}_e$ essentially change only on grounds of fluid-dynamical effects on fluid timescales, the latter being longer than the radiative timescale $\tau_{\rm adv} \sim \Delta x/c$ used for time integration. Conversely, an explicit treatment of $\hat{e}_{\rm i}$ and $\hat{n}_e$ would not be feasible if we would integrate the radiation moment equations fully implicitly using a time step longer than $\sim \Delta x/v$ (as it is done, for instance, in most existing neutrino-hydrodynamics codes using FLD or a Boltzmann-solver). Additionally, it is worth to note that although an explicit treatment of $\hat{e}_{\rm i}$ and $\hat{n}_e$ may slightly reduce the accuracy it does not significantly harm the numerical stability of the overall scheme, because the effective source terms for $\hat{e}_{\rm i}$ and $\hat{n}_e$ are computed via Eqs. (13) using the time-discretized source terms for $\hat{E}_{\nu,\xi}$, which themselves result from an implicit (and hence stable) integration in $\hat{E}_{\nu,\xi}$.

Once after appropriately time-discretized expressions for the source terms of the 1st radiation moments are found, the changes of the fluid-momentum and kinetic-energy densities due to momentum transfer with neutrinos obtained using Eq. (13b) as:

$$\left(\delta_t \hat{\rho}\hat{v}^i\right)_{\rm src} = -\frac{1}{c^2}\sum_{\nu,\xi}\left(\delta_t \hat{F}^i_{\nu,\xi}\right)_{\rm src}\,, \tag{61a}$$

$$(\delta_t \hat{e}_{\rm k})_{\rm src} = -\frac{\hat{v}_j}{c^2}\sum_{\nu,\xi}\left(\delta_t \hat{F}^j_{\nu,\xi}\right)_{\rm src}\,. \tag{61b}$$

Finally, since this is a non-trivial and important aspect, we now demonstrate that the time-integration algorithm presented in Sec. 3.3 in combination with the stiffness-parameter dependent flux formulation, Eq. (50), allows the radiation flux $\boldsymbol{F}$ in diffusive regions (in which $\mathcal{P} \gg 1$) to relax to the corresponding diffusive flux $\boldsymbol{F}_{\rm D} \equiv -c\nabla E/(3\kappa_{\rm tra})$ in a numerically stable and non-oscillatory manner. To this end, we may neglect velocity-dependent terms – which are reduced by a factor of $\mathcal{O}[(v/c)(1/\mathcal{P})]$ compared to the dominant terms in our comoving-frame formulation and therefore subdominant in the diffusion regime – and we only consider the (usually dominant) emission-/absorption and isoenergetic scattering reactions, for which the 1st-moment source terms can be written as $(\delta_t \boldsymbol{F})_{\rm src} = -c\kappa_{\rm tra}\boldsymbol{F}$. Since in the diffusion regime we expect the pressure tensor to be almost isotropic, $P^{ij} \simeq \delta^{ij}E/3$, the hyperbolic operator for the flux density then reads exemplarily in x-direction (cf. Eqs. (49), (50)):

$$\begin{aligned}(\delta_t \hat{F}^x_{\rm i})^{\rm n}_{\rm hyp} &= \frac{c^2}{3\Delta V_{\rm i}}\left(\Delta A_{{\rm i}+\frac{1}{2}}\frac{\hat{E}^{\rm L}_{{\rm i}+\frac{1}{2}}+\hat{E}^{\rm R}_{{\rm i}+\frac{1}{2}}}{2} - \Delta A_{{\rm i}-\frac{1}{2}}\frac{\hat{E}^{\rm L}_{{\rm i}-\frac{1}{2}}+\hat{E}^{\rm R}_{{\rm i}-\frac{1}{2}}}{2}\right)\\ &\simeq -c\hat{\kappa}_{\rm tra}(\hat{F}^x_{\rm D})^{\rm n}_{\rm i}\,,\end{aligned} \tag{62}$$

where $\hat{F}^x_{\rm D}$ is a proper numerical representation of the diffusive flux $F^x_{\rm D}$. The first partial update (step *4)* in Sec. 3.3) for $\hat{\boldsymbol{F}}$ then results to:

$$\begin{aligned}\hat{\boldsymbol{F}}^{{\rm n}+\frac{1}{2}} &= \hat{\boldsymbol{F}}^{\rm n} + \Delta t^*\left[-(\delta_t\hat{\boldsymbol{F}})^{\rm n}_{\rm hyp} + (\delta_t\hat{\boldsymbol{F}})^{{\rm n}+\frac{1}{2}}_{\rm src}\right]\\ &\simeq \hat{\boldsymbol{F}}^{\rm n} + c\hat{\kappa}_{\rm tra}\Delta t^*\,\hat{\boldsymbol{F}}^{\rm n}_{\rm D} - c\hat{\kappa}_{\rm tra}\Delta t^*\,\hat{\boldsymbol{F}}^{{\rm n}+\frac{1}{2}}\\ &\simeq \frac{\hat{\boldsymbol{F}}^{\rm n}}{1+c\hat{\kappa}_{\rm tra}\Delta t^*} + \frac{c\hat{\kappa}_{\rm tra}\Delta t^*\,\hat{\boldsymbol{F}}^{\rm n}_{\rm D}}{1+c\hat{\kappa}_{\rm tra}\Delta t^*}\,,\end{aligned} \tag{63}$$

where $\Delta t^* \equiv \Delta t/2$. Hence, for $c\kappa_{\rm tra}\Delta t^* \gg 1$ the flux density $\hat{\boldsymbol{F}}$ consistently relaxes to $\hat{\boldsymbol{F}}_{\rm D}$ within one (partial) time step without any numerical overshooting.

3.7 Hydrodynamics

The equations of hydrodynamics are integrated using the finite-volume high-resolution shock-capturing scheme developed in Obergaulinger (2008). The scheme evolves the conserved hydrodynamic variables $(\rho, \rho\boldsymbol{v}, e_{\rm t})$, to which end a variety of procedures for spatial reconstruction (cf. Sec. 3.2) and Riemann solvers (Lax-Friedrich, HLL, HLLC, HLLD, see, e.g., Toro 1997) can be selected. Moreover, a magnetic-field solver and various models of viscosity and magnetic diffusivity are implemented. In the case of the model setup requiring the co-evolution of a set of different fluid species a simplified version of the "Consistent Multifluid Advection" scheme (Plewa & Müller 1999) is utilized. For more details about the non-radiative part of the code, we refer the reader to Obergaulinger (2008).

4 TEST PROBLEMS

In this section, we present a variety of problems to test the methods described in the previous sections. Several idealized, non-microphysical tests in 1D and 2D are performed which, although they are not directly related to typical scenarios where neutrino transport plays a role, serve to assess the quality of the two-moment closure approximation and the coupling of the radiation moments to the velocity field and to the hydrodynamics part of the code. Subsequently, we present two one-dimensional test problems related to CCSNe in which we test the AEF scheme both for different closure prescriptions and against corresponding results from FLD and Boltzmann schemes.

In order to avoid excessive repetitions we list some recurring properties and parameters that various following tests are equipped with:

- Regarding the numerical treatment, we employ a 5th-order MP reconstruction method and an HLL Riemann solver for both the radiation transport and the hydrodynamics part of the system. For the tests in 1D we take a global CFL factor of CFL= 0.7 while for the 2D tests we set CFL= 0.5.
- We apply boundary conditions (BCs) by fixing the values in the boundary (ghost) zones surrounding the computational domain according to a given prescription. For a reflective boundary, e.g. at $x = x_0$, we copy scalar quantities, e.g. $E|_{x_0+\delta x} = E|_{x_0-\delta x}$, and apply the reflection operator to vectorial quantities, e.g. $(F^x, F^y, F^z)|_{x_0+\delta x} =$

[12] www.nag.co.uk

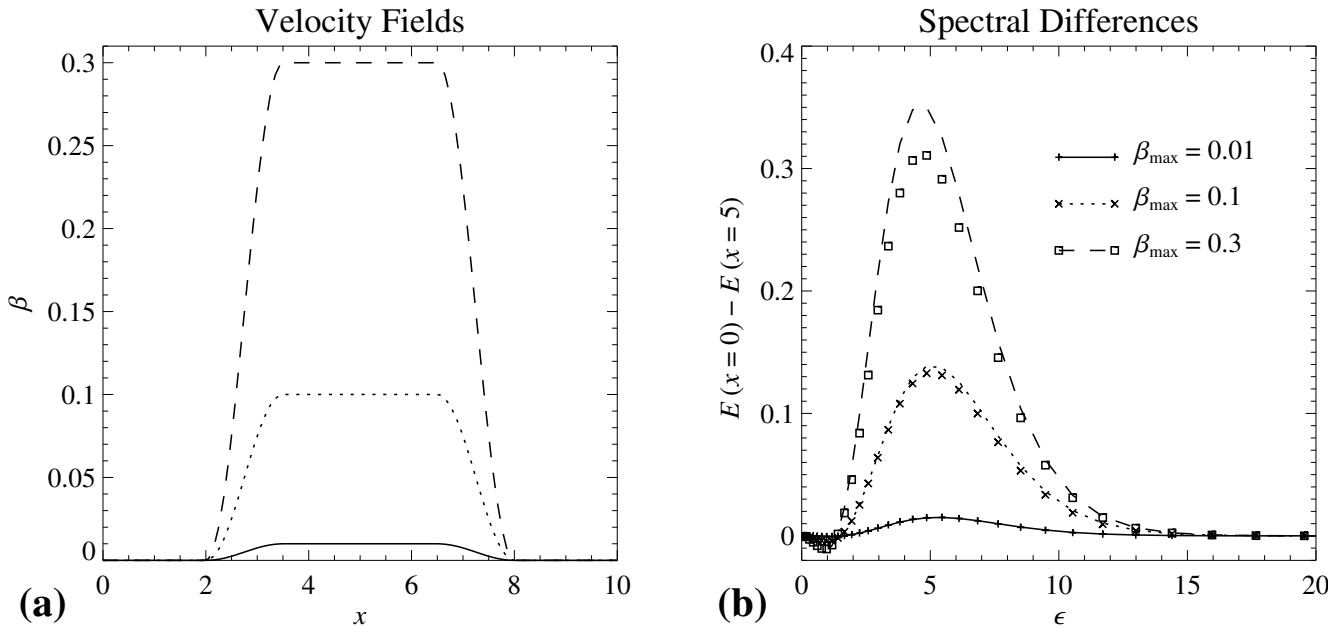

Figure 1. Doppler shift of free-streaming radiation. Panel (a) shows the three velocity fields as functions of the location x and panel (b) depicts the differences between the energy distributions in the two frames with $\beta = 0, \beta_{\max}$. The lines denote the fully relativistic, analytic solutions, while the symbols show the AEF results.

$(-F^x, F^y, F^z)|_{x_0-\delta x}$. For a non-reflective outflow boundary, e.g. at $x = x_0$ we employ the usual 0th-order extrapolation for all quantities, e.g. we set $E(x_0 + \delta x) = E(x_0)$.

- In all of the subsequent tests in which dimensionless equations and quantities are employed the speed of light is set to $c = 1$ and for the velocity the symbol β is used.
- Except for the tests in Secs. 4.1.3, 4.3.1 and 4.3.2, we will exclusively use the Minerbo closure, which is expressed by the Eddington factor as in Eq. (28a) and the 3rd-moment factor as in Eq. (33).

4.1 One-dimensional idealized test problems

4.1.1 Doppler shift of free-streaming radiation

The energy-coupling scheme describing the Doppler shift (cf. Sec. 3.5.3) can immediately be tested by comparing the spectra of a free-streaming radiation field in two different frames with non-vanishing relative velocity. We adopt the basic setup from Vaytet et al. (2011), but we use dimensionless units and take higher values for the maximum velocities $\beta_{\max} \in \{0.01, 0.1, 0.3\}$. The Cartesian spatial domain covers $x \in [0, 10]$ and is resolved by 100 equidistant grid points, while the energy space is discretized between $\epsilon \in [0, 50]$ using a logarithmic grid with 40 bins and a bin-enlargement factor of $\Delta\epsilon_{\xi+1}/\Delta\epsilon_\xi = 1.1$. At $x = 0$ we inject a beam of radiation by fixing the radiation quantities in the boundary zones according to $E(x = 0) = \epsilon^3/(\mathrm{e}^\epsilon - 1) = F(x = 0)$. The boundary at $x = 10$ is set to outflow. The radiation field traverses velocity fields with the shape of smoothed step-functions as shown in panel (a) of Fig. 1. Within regions where $\beta > 0$ the redshifted (i.e. Lorentz-boosted) spectrum of the comoving-frame specific energy density is analytically given by

$$E_\beta = \frac{1}{s}\frac{(s\epsilon)^3}{\mathrm{e}^{s\epsilon} - 1}, \quad \text{where } s \equiv \sqrt{\frac{1+\beta}{1-\beta}}, \tag{64}$$

which is valid for $0 \leqslant \beta \leqslant 1$.

The differences between the spectra in the frames $\beta = 0, \beta_{\max}$ for both our numerical and the analytic solution are shown in panel (b) of Fig. 1. The Doppler shift is captured well by our scheme: The agreement with the analytic solution converges for decreasing values of $\beta_{\max}$. For high velocities, $\beta_{\max} = 0.3$, the $\mathcal{O}(v/c)$ approximation leads to errors of about 10 % with respect to the relativistic solution.

4.1.2 Differentially expanding isothermal atmosphere

To test the algebraically closed two-moment transport in combination with frame-dependent effects and (idealized) radiation–matter interactions we examine a scenario that was also investigated by Mihalas (1980) (in full relativity) and by Rampp & Janka (2002) (in $\mathcal{O}(v/c)$), both using accurate Boltzmann techniques. The scenario includes an expanding, isothermal atmosphere that expands with velocity *beta* as function of radius r as

$$\beta(r) = \beta_{\max}\frac{r - r_{\min}}{r_{\max} - r_{\min}} \tag{65}$$

and which exhibits an absorption opacity κ_a that varies in r and (photon) energy ϵ as

$$\kappa_\mathrm{a}(r, \epsilon) = \begin{cases} \frac{10\alpha}{r^2}\mathrm{e}^{-(\epsilon-\epsilon_0)^2/\Delta^2} + \frac{\alpha}{r^2}\left(1 - \mathrm{e}^{-(\epsilon-\epsilon_0)^2/\Delta^2}\right) & , \epsilon \leqslant \epsilon_0 \\ \frac{10\alpha}{r^2} & , \epsilon > \epsilon_0 \,. \end{cases} \tag{66}$$

That is, for fixed radius r, the opacity is a smoothed step-function in energy space with the transition at energy ϵ_0 from a low opacity to a 10 times higher opacity with transition width Δ. The model parameters are

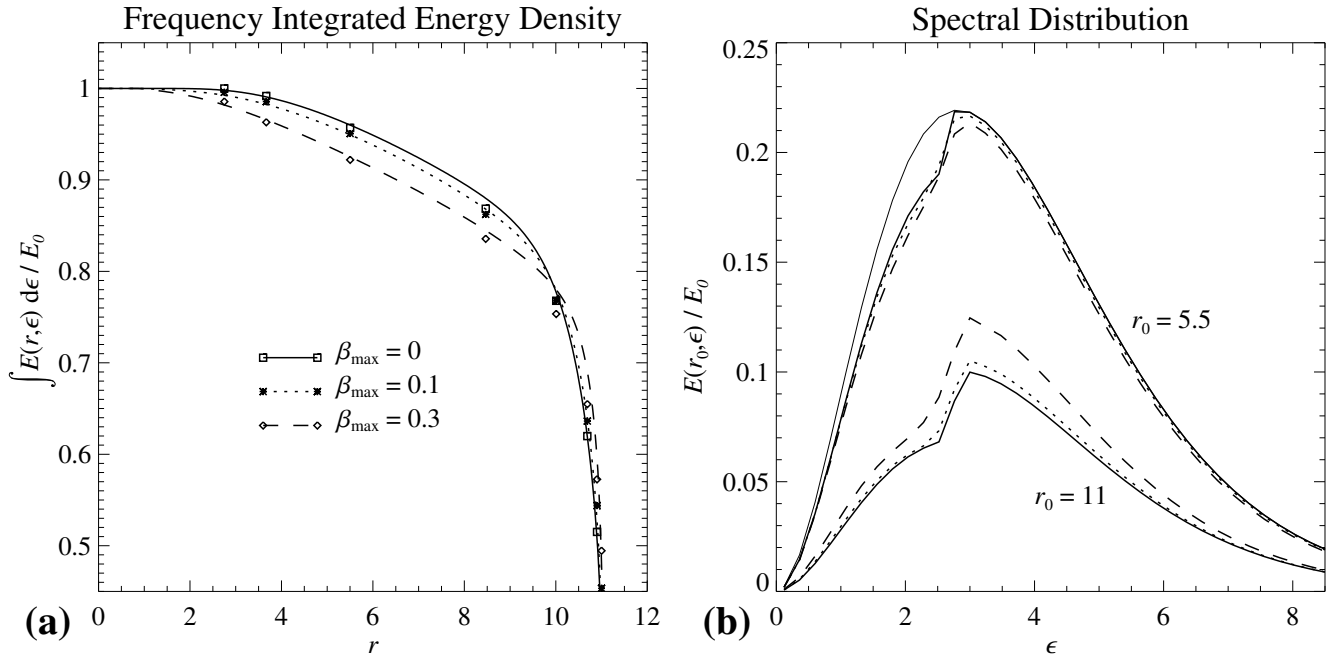

Figure 2. Differentially expanding isothermal atmosphere. In panel (a) the frequency-integrated energy densities, normalized by $E_0 \equiv \bar{E}(r=0)$, as function of radius are shown for different maximum velocities $\beta_{\max}$. The symbols denote the reference solution computed by Mihalas (1980), where the points are read off their Fig. 5. In panel (b) we show for the same models the spectral distributions of the normalized energy densities at the two radii $r = 5.5$ and 11, at which the optical depth for photons with energy $\epsilon < \epsilon_0$ is ≈ 1 and ≈ 0, respectively. The thin solid line displays the equilibrium distribution $E^{\mathrm{eq}}(\epsilon)$.

$\{r_{\min}, r_{\max}, \epsilon_0, \Delta, \alpha\} = \{1, 11, 3, 0.2, 10.9989\}$ and the maximum velocity $\beta_{\max}$ is varied between $\beta_{\max} \in \{0, 0.1, 0.3\}$. We use dimensionless units in which the temperature $T = 1$ such that the photon equilibrium energy density is given by $E^{\mathrm{eq}}(\epsilon) = \epsilon^3/(\mathrm{e}^{\epsilon} - 1)$. We set up a uniform radial grid of 400 zones to cover a region of $r \in [0.1, 15]$. The additional (with respect to the reference calculations) region $[11, 15]$, wherein the opacities are set to zero, merely serves as a transition zone for the radiation field to reach near free-streaming conditions in order to avoid unphysical feedback from the outer radial boundary, at which outflow BCs are employed. At $r = 0.1$, a reflective BC is applied. The energy grid is composed of 50 equidistant bins within $\epsilon \in [0, 12]$.

For comparison, we show similar plots as in Rampp & Janka (2002), see Fig. 2. The total radiation energy density as function of radius is shown in panel (a), while the radiation spectrum at two representative radii is shown in panel (b). A remarkable fact is that the case with no expansion is already reproduced well with an accuracy of $\lesssim 1\%$ by the approximate AEF scheme. By switching to $\beta > 0$ we introduce the following effects: Due to the expansion the comoving-frame energy- and flux densities of photons created deeper within the atmosphere decreases on their way to the surface, as can be seen by monotonic decline of the energy densities with increasing $\beta_{\max}$ up to $r \approx 10$. However, this trend is competed by the effect that the overall fraction of photons originally created in the high-opacity band is lifted with increasing velocity (and radius), since a fraction of photons are redshifted from $\epsilon > \epsilon_0$ to $\epsilon < \epsilon_0$ on their way to the surface. Hence, the opacity jump is effectively redshifted by the expansion, leading to higher integral values of the energy density at $r \gtrsim 10$. Both effects are captured well by the AEF method. We notice an increasing difference between the $\mathcal{O}(v/c)$ results and the fully relativistic results for increasing $\beta_{\max}$. However, for $\beta_{\max} = 0.3$ the maximum error in the integral energy density, cf. panel (a) of Fig. 2, is still less than $\sim 5\,\%$.

4.1.3 Supercritical radiative shock

Successively increasing the degrees of freedom taken into account, we now turn to a classical RHD problem to test the accurate coupling between transport and hydrodynamics, the radiative shock tube. Having been the subject of numerous investigations, both analytically (e.g Zeldovich & Raizer 1966; Mihalas & Mihalas 1984) and numerically (e.g. Ensman 1994; Sincell et al. 1999), radiative shock tubes repeatedly served as test problems for the development of new RHD codes as, e.g., in Turner & Stone (2001); Hayes & Norman (2003); González et al. (2007); Vaytet et al. (2011); Jiang et al. (2012); Skinner & Ostriker (2013).

Since the detailed physical description of radiative shocks is out of the scope of our presentation, we only briefly summarize their essential properties here. In contrast to purely hydrodynamic shocks radiative shocks allow for energy transfer between the gas and radiation, effectively introducing cooling of the post-shock and heating of the pre-shock material. Depending on the shock velocity, heating of upstream material in front of the shock – this region is called radiative precursor – can become so efficient that the pre-shock temperature adapts to the post-shock temperature, in which case the shock is called a supercritical radiative shock. In this case, both the up- and downstream material is in radiative equilibrium close to the shock and separated

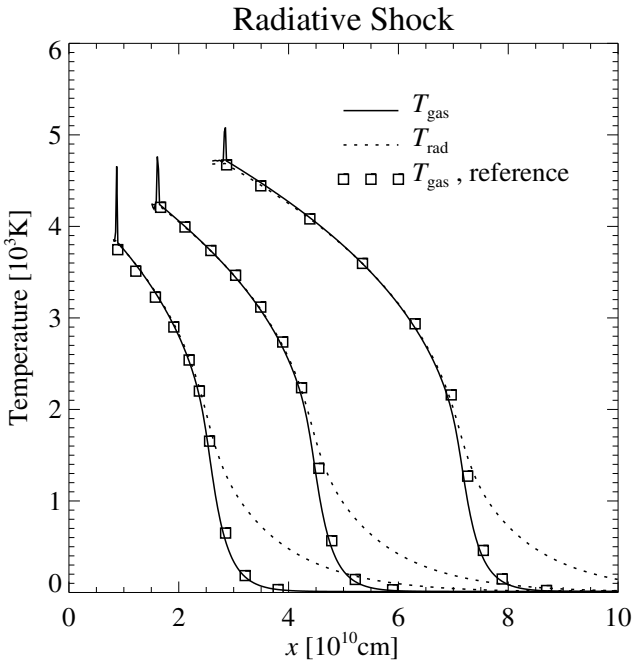

Figure 3. Supercritical radiative shock. We show the gas and radiation temperatures at three different times $t \in \{4\times10^3, 7.5\times10^3, 1.3\times10^4\}$ s. Each curve is plotted in the frame in which the shock crosses $x = 0$ at $t = 0$ with a velocity $v_{\rm s} = 2\times10^6\,{\rm cm\,s^{-1}}$. The square symbols denote points from the reference calculation by Vaytet et al. (2011), which have been read off their Fig. 9.

by a sharp non-equilibrium temperature spike ("Zeldovich spike"), which is roughly as wide as the local mean-free path of radiation.

We initialize our model of a supercritical radiative shock using the same setup as Vaytet et al. (2011), who also employed a spectral AEF scheme fairly similar to ours. Moreover, to facilitate the comparability with Vaytet et al. (2011) we apply the M_1 instead of the Minerbo closure for this test. The only difference to the setup of Vaytet et al. (2011) is that we ignore here the 3rd-moment terms in the evolution equation for the 1st moment (i.e. the (IV)-terms in Eq. (7b)). However, these terms vanish in the energy-integrated form of the RHD equations and the fluid quantities, such as the temperature, should not be significantly influenced by this measure, particularly in view of the relatively low velocities at hand. A Cartesian box of length 10^{11} cm is discretized by a uniform grid of 500 cells and initially homogeneously filled with gas of density $\rho = 7.78\times10^{-10}\,{\rm g\,cm^{-3}}$, temperature $T = 10\,{\rm K}$ and grey absorption opacity $\kappa_{\rm a} = 3.1\times10^{-10}\,{\rm cm^{-1}}$. Initially, radiation is everywhere in equilibrium with the gas, such that $\bar{E} = \bar{E}^{\rm eq} = a_{\rm rad}T^4$, where $a_{\rm rad} \approx 7.57\times10^{-15}{\rm erg\,cm^{-3}\,K^{-4}}$ is the radiation constant. The gas pressure is computed as $P_{\rm g} = (\gamma_{\rm gas}-1)e_{\rm i} = \rho k_{\rm B}T/m_{\rm B}$ with $\gamma_{\rm gas} = 1.4$. We take the frame of the shock moving with $v_{\rm s} = 2\times10^6\,{\rm cm\,s^{-1}}$ relative to its preceding medium as our simulated inertial frame. To this end, we let all matter in the computational domain initially move with velocity $v = -v_{\rm s}$. The shock is induced by using a reflective boundary at $x = 0$ and it is maintained by feeding new material with the original properties at $x = 10^{11}$ cm into the computational domain. We discretize the frequency space with $N_\epsilon = 8$ evenly spaced bins between $\epsilon \in [0, 8\times10^{14}]$ Hz.

The results are shown in Fig. 3 in form of the distributions of the gas temperature $T_{\rm gas}$ and the radiation temperature, the latter being defined as $T_{\rm rad} \equiv (\bar{E}/a_{\rm rad})^{1/4}$. Using an essentially similar physical evolution model as Vaytet et al. (2011), the results we obtain with our quasi-explicit numerical method are in good agreement with the outcome of their implicit radiation solver which shows that the coupling between the radiative and hydrodynamics systems is numerically robust and produces accurate results.

4.2 Two-dimensional idealized test problems

4.2.1 Shadow casting problem

We begin our presentation of 2D test problems with a rather qualitative test that puts one of the generic advantages of a two-moment scheme into focus, namely the ability of an opaque object to generate a shadow when being illuminated by radiation. In a two-moment scheme, the flux-density vector is an evolved quantity, and the pressure tensor is generally non-isotropic. In contrast, in an FLD scheme (see Sec. 2.4.1), the flux direction is determined by the gradient of the scalar energy density, which corresponds to an isotropic radiation pressure. This leads to the unphysical effect that in the free-streaming regime, $f \to 1$, anisotropic features of the radiation field, such as shadows, cannot be maintained and are quickly washed out.

As it has likewise been done before for various other radiative transfer/transport codes (see e.g. Audit et al. 2002; Hayes & Norman 2003; Iliev et al. 2006; Skinner & Ostriker 2013, and references therein) we set up a purely absorbing gas cloud which is exposed to near free-streaming radiation to test the ability of radiation to cast a shadow behind the gas cloud. Specifically, in a Cartesian domain with $\boldsymbol{x} \equiv (x, y) \in [0, 15]\times[-5, 5]$ and resolved by $N_x \times N_y = 300\times200$ cells, we define one region in which the radiation field is generated, the circular region $\mathcal{S}$ centered around $\boldsymbol{x}_{\mathcal{S}} = (3, 0)$ with radius $r_{\mathcal{S}} = 3/2$, and we define another circular region $\mathcal{A}$ centered around $\boldsymbol{x}_{\mathcal{A}} = (11, 0)$ with radius $r_{\mathcal{A}} = 2$ to be the purely absorbing cloud. The absorption opacity $\kappa_{\rm a}$ and equilibrium energy density $E^{\rm eq}$ are defined as follows:

$$\kappa_{\rm a}(\boldsymbol{x}) = \begin{cases} 10\exp\{-(4|\boldsymbol{x}-\boldsymbol{x}_{\mathcal{S}}|/r_{\mathcal{S}})^2\} & , \boldsymbol{x}\in\mathcal{S} \\ 10 & , \boldsymbol{x}\in\mathcal{A} \\ 0 & , \text{else} \end{cases}, \tag{67a}$$

$$E^{\rm eq}(\boldsymbol{x}) = \begin{cases} 10^{-1} & , \boldsymbol{x}\in\mathcal{S} \\ 0 & , \text{else} \end{cases}. \tag{67b}$$

The model is initialized with vanishing flux densities and a homogeneous distribution of negligibly small energy densities.

From the numerical point of view, the present objective is to test the correct implementation of the multidimensional hyperbolic part of the radiation moment equations, particularly of the angular dependence of the signal speeds in the Riemann solver, cf. Eqs. (47). The signal speeds determine the numerical fluxes between grid cells, cf. Eq. (48), and close to free-streaming conditions both the signal speeds as well as the intercell fluxes should be strongly suppressed orthogonal to the direction of the radiation flux.

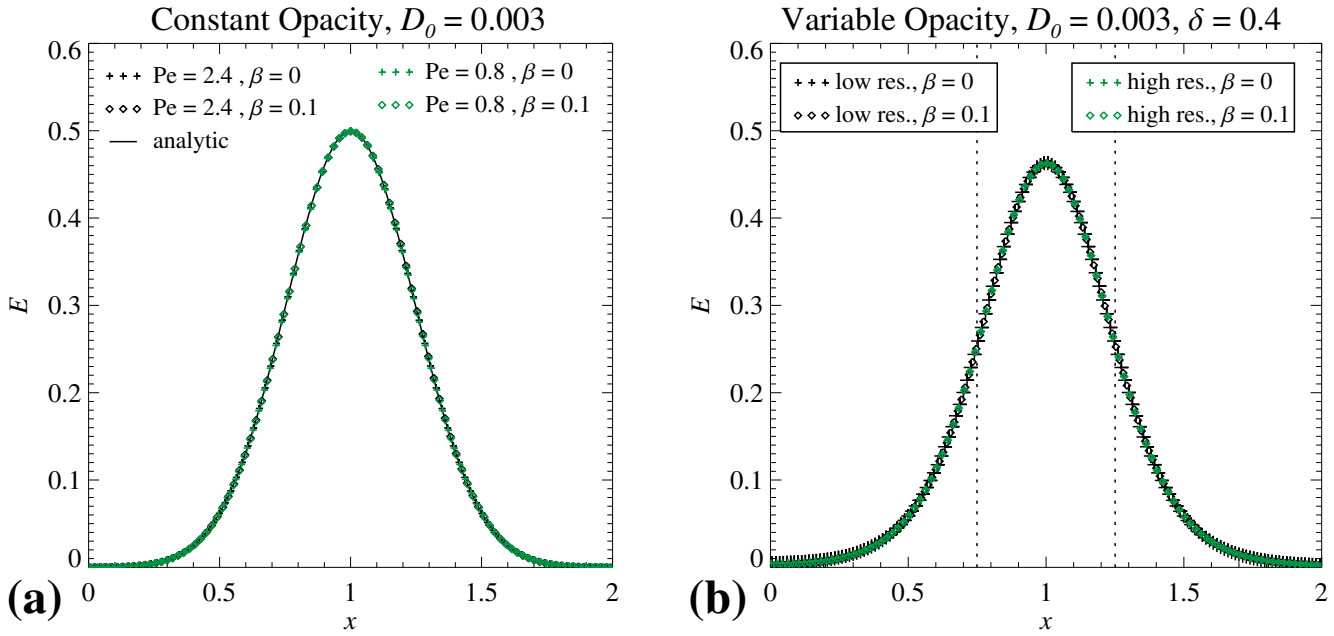

Figure 5. Static and dynamic diffusion. We show profiles of the energy densities along the slice $y = 1$ after the simulation time $t - t_0 = 5$ of the Gaussian pulse centered at $\boldsymbol{x}_0 = (1, 1)$. In panel (a) the results for the cases with spatially constant opacity are plotted. The models differ in spatial resolution, and therefore in the stiffness parameters $\mathcal{P}$, and in the uniform velocity field parallel to the x-direction with magnitude β. The results for the cases with $\beta > 0$ were transformed to the $\beta = 0$ frame and shifted to their initial position at $t = 0$. For a better readability, only every second zone value is plotted for the high-resolution models. The results shown in panel (b) are produced by the same initial Gaussian pulse but employing an opacity that declines with distance to the center of the pulse. The vertical lines denote the locations where the stiffness parameter of the low-resolution models is $\mathcal{P} = 1$. In the high-resolution models, the stiffness parameter is $\mathcal{P} < 1$ everywhere.

The three snapshots in Fig. 4 show for three consecutive times contours of the isotropic luminosity L emitted by the source, given in this two-dimensional geometry by $L = 2\pi r_c |\boldsymbol{F}|$ with $r_c \equiv |\boldsymbol{x} - \boldsymbol{x}_S|$. One can see that a clearly obscured region behind the gas cloud emerges. The luminosity behind the gas cloud is not an ideal step-function in vertical direction but it changes rather continuously within a fan of opening angle $\approx 20^\circ - 30^\circ$. The reasons for this are, first, that radiation is not emitted from a point-like but a spatially extended source, causing the flux-factor to be $|\boldsymbol{F}|/E \sim 0.98 < 1$ at $r_c = 8$, and second, that the gas cloud is not perfectly absorbing but has a finite value of κ_a, which allows a small fraction of radiation to pass through the gas cloud near its edges. Altogether our code performs well in this test, the development and propagation of the multidimensional radiation field and its particular feature to cast a shadow are consistently captured.

4.2.2 Static and dynamic diffusion

A standard test for radiation codes allowing for the treatment of optically thick regions (e.g. González et al. 2007; Swesty & Myra 2009) is the scenario of an initially concentrated bulge of radiation diffusing into its environment. Being conceptually based on the diffusion limit, an FLD scheme usually performs well in this test, as long as the medium is sufficiently opaque. On the other hand, in a two-moment AEF scheme the diffusion equation only results in the parabolic limit of the otherwise hyperbolic equations. Therefore, it has to be checked that the numerical method chosen to solve the AEF scheme consistently describes the parabolic diffusion limit and that the transition to the hyperbolic regime proceeds in a numerically stable and accurate fashion (cf. Secs. 3.4 and 3.6). Concerning the last point, we explicitly want to ensure that no spurious, resolution-dependent features result from modifying the numerical fluxes whenever the local stiffness parameter exceeds unity, cf. Eq. (50). Finally, in this setup we also want to test the ability of the algorithm to accurately describe dynamic diffusion, i.e. diffusion out of a moving medium.

We perform a set of calculations in a Cartesian box given by $\boldsymbol{x} \equiv (x, y) \in [0, 3] \times [0, 2]$. All configurations are initialized at a fiducial time $t_0 = 5$ with the following Gaussian pulse of radiation energy density and corresponding diffusive flux density centered around $\boldsymbol{x}_0 = (1, 1)$:

$$E(\boldsymbol{x}, t_0) = E_0 \exp\left\{-\frac{|\boldsymbol{x} - \boldsymbol{x}_0|^2}{4D_0}\right\}, \quad \boldsymbol{F}(\boldsymbol{x}, t_0) = -D_0 \nabla E, \tag{68}$$

where $E_0 = 1$ and $D_0 = 3 \times 10^{-3}$.

In the first configuration we define a spatially constant diffusion coefficient, $D \equiv (3\kappa_s)^{-1} = D_0$, which allows us to compare the numerical results with an analytic solution, given by:

$$E(\boldsymbol{x}, t) = E_0 \frac{t_0}{t_0 + t} \exp\left\{-\frac{|\boldsymbol{x} - \boldsymbol{x}_0|^2}{4D_0(t_0 + t)}\right\}. \tag{69}$$

For this configuration we switch between two resolutions $\{N_x, N_y\} = \{450, 300\}$ and $\{150, 100\}$ corresponding to which the stiffness parameters, $\mathcal{P} = \kappa_s \Delta x$, are lower and greater than 1, respectively. Additionally, for both resolu-

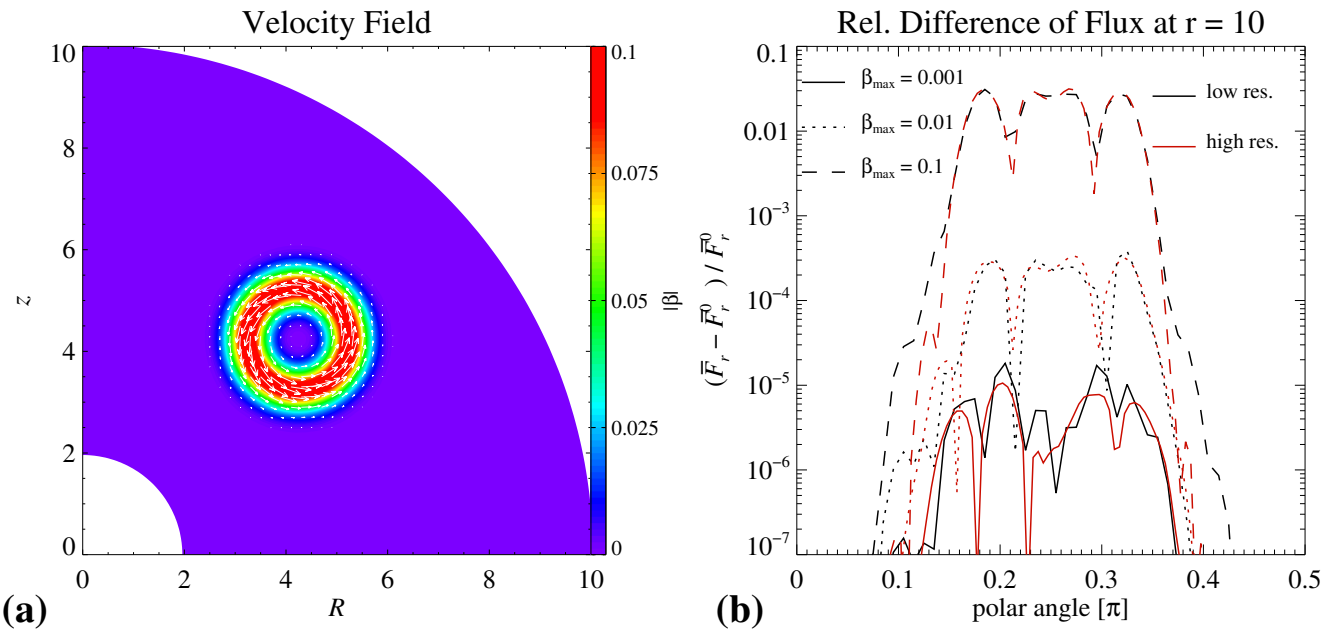

Figure 6. Radiation traversing variable velocity fields. In panel (a) we show the absolute value (color coded) of the velocity and its polar component (arrows) for the high-velocity case with $\beta_{\max} = 0.1$. In panel (b) we plot the relative difference of the energy-integrated radial flux density, $\bar{F}_r$, with respect to the case of vanishing velocity, $\bar{F}_r^0$, measured at radius $r = 10$ as function of polar angle.

tions we vary between a vanishing and a non-vanishing spatially constant velocity in x-direction, i.e. $\beta = 0$ and 0.1, respectively. For comparison with the $\beta = 0$ models, we plot the radiation energy densities of the $\beta > 0$ models in the coordinate frame of the $\beta = 0$ models.

In panel (a) of Fig. 5, we see that after a simulation time of $t - t_0 = 5$, when the maximum value of E has reached about half of its initial value $E_0 = 1$, all models agree well with the analytic solution and we cannot identify unphysical numerical features in any of the different cases.

We consider a second configuration with the same initial conditions, cf. Eqs. (68), to test the correct transition from a stiff ($\mathcal{P} > 1$) to a non-stiff ($\mathcal{P} < 1$) regime. To this end, instead of a constant opacity we now use a variable opacity that declines with distance from the center as

$$\kappa_{\rm s}(\boldsymbol{x}) = \frac{1}{3D_0} \exp\left\{-\frac{|\boldsymbol{x} - \boldsymbol{x}_0|^2}{\delta^2}\right\} \tag{70}$$

on a length scale of $\delta = 0.4$. We display the results at the simulation time $t - t_0 = 5$ in panel (b) of Fig. 5. We again compare four cases with two resolutions, $\{N_x, N_y\} = \{450, 300\}$ and $\{225, 150\}$, and two homogeneous velocities in x-direction $\beta = 0$ and 0.1. For the models with $\beta > 0$, the opacity profile is advected with the fluid, i.e. the opacity $\kappa_{\rm s}^{\beta}(\boldsymbol{x}, t) \equiv \kappa_{\rm s}(\boldsymbol{x} - \beta t)$ is employed. In the high-resolution cases, which serve as references for the low-resolution cases, the stiffness parameter is $\mathcal{P} < 1$ everywhere, while in the low-resolution cases the stiffness parameter crosses $\mathcal{P} = 1$ at the locations indicated by the dotted lines. We observe no numerical artifacts near the transition where $\mathcal{P} = 1$ in the low-resolution cases, which indicates that the modification of the numerical fluxes, Eq. (50), works accurately.

4.2.3 Radiation traversing variable velocity fields

Since the quantities $E, \boldsymbol{F}$ evolved in our two-moment formulation are defined in the comoving frame, they are subject to variations whenever radiation crosses regions of variable velocity even without any interactions present. The net impact on the radiation properties after passing such regions and returning back into the original frame would vanish in an exact calculation. In practice, however, we encounter two limitations that spoil this feature to be fulfilled precisely: First, our underlying scheme for the radiation moments neglects all contributions of order $\mathcal{O}(v^2/c^2)$ in both evolution equations, which results in a loss of the property that a transformation from one frame to another is exactly reversible – instead such a transformation generates errors of the disregarded order $\mathcal{O}(v^2/c^2)$. The second reason is that we do not solve the evolution equations exactly but only numerically, i.e. all our solutions are beset with truncation errors depending on the spatial and temporal resolution and on the numerical algorithm.

In order to obtain a qualitative impression of how strongly both aforementioned effects can impact the solution, we set up an arbitarily shaped velocity field and let it be traversed by a spherically expanding radiation field. The radiation field is induced at the boundary at radius $r = 2$ with an energy density of $E(\epsilon) = \epsilon^3/(\mathrm{e}^{\epsilon} - 1)$, a radial flux density of $F_r(\epsilon) = E(\epsilon)/2$, and vanishing non-radial flux components, $F_\theta = F_\phi = 0$. The energy grid consists of $N_\epsilon = 10$ bins logarithmically distributed between $\epsilon \in [0, 30]$ with an enlargement factor $\Delta\epsilon_{\xi+1}/\Delta\epsilon_\xi = 1.3$. The velocity field in the polar plane, $\boldsymbol{v}_{\rm pol}$, represents an eddy with radius $d_1 = 1$ circulating around its center at $\boldsymbol{x}_0 = (5, 5)/\sqrt{2}$, while the toroidal velocity field $\boldsymbol{v}_{\rm tor}$ has the same absolute magnitude as the poloidal field but points into the ϕ-direction.

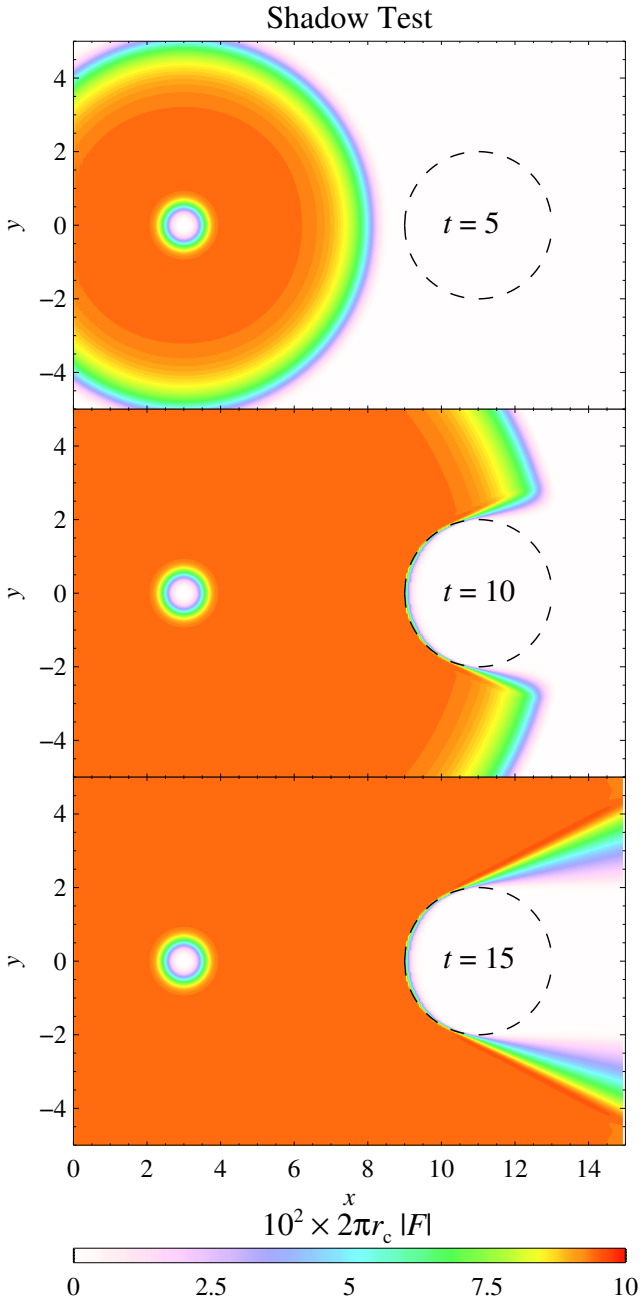

Figure 4. Shadow casting problem. The 2D luminosity at the three indicated times t is plotted. The dashed line indicates the boundary of the absorbing gas cloud.

Explicitly, we set

$$\boldsymbol{v}_{\rm pol} = \frac{\beta(\boldsymbol{x})}{\sqrt{2}}\mathbf{e}_{\rm pol} \quad , \quad \boldsymbol{v}_{\rm tor} = \frac{\beta(\boldsymbol{x})}{\sqrt{2}}\mathbf{e}_{\phi}\,, \tag{71}$$

with

$$\beta(\boldsymbol{x}) = \beta_{\rm max}\exp\left\{-(|\boldsymbol{x}-\boldsymbol{x}_0|-d_1)^2/d_2^2\right\}\,, \tag{72}$$

where $d_2 = 0.4$, $\mathbf{e}_\phi$ is the unit vector in ϕ-direction, and $\mathbf{e}_{\rm pol}$ is the unit vector perpendicular to both $\boldsymbol{x}-\boldsymbol{x}_0$ and $\mathbf{e}_\phi$ and signed such to point in clockwise direction in the $R-z$ plane (see panel (a) of Fig. 6). We vary the maximum value of the velocity between $\beta_{\rm max} \in \{10^{-3}, 10^{-2}, 10^{-1}\}$ and we use the two spatial resolutions $N_r = N_\theta \in \{50, 100\}$ between $r \in [2, 10]$ and $\theta \in [0, \pi/2]$. At $r = 10$ we employ an outflow BC.

In panel (b) of Fig. 6 we compare the energy-integrated fluxes $\bar{F}_r$ obtained for each velocity field and resolution with the corresponding value $\bar{F}_r^0$ resulting for a vanishing velocity field. If the two shortcomings mentioned in the beginning of this section were absent, both fluxes would be exactly equal, i.e. $(\bar{F}_r - \bar{F}_r^0)/\bar{F}_r^0 = 0$. Instead, in our numerical calculation we receive relative errors of up to $(\bar{F}_r - \bar{F}_r^0)/\bar{F}_r^0\big|_{\rm max} \sim \{4\times10^{-2}, 4\times10^{-4}, 1\times10^{-5}\}$ for $\beta_{\rm max} = \{10^{-3}, 10^{-2}, 10^{-1}\}$. The outcome that the lines lie much closer together for different resolutions than for different $\beta_{\rm max}$ shows that the low resolution already sufficiently resolves the solution corresponding to the underlying moment equations, at least for $\beta_{\rm max} > 10^{-3}$. It can further be observed that the leading-order error term representing missing components compared to the fully relativistic formulation is not $\mathcal{O}(v/c)$, as can be inferred from the tendency of relative differences to roughly decrease by two orders of magnitude for a one-order reduction of $\beta_{\rm max}$. Hence, we deduce that in our implementation no significant contributions of order $\mathcal{O}(v/c)$ are missing or are erroneously present since in any other case we would have found an error scaling linearly with $\beta_{\rm max}$.

4.3 One-dimensional problems including microphysics

While the previous test problems are based on rather idealized setups, the two remaining one-dimensional test problems specifically focus on neutrino transport in CCSNe. In particular, the tests should address the question how the AEF scheme performs compared to the present standard methods, the FLD and the Boltzmann-type solvers. To this end, in the first test in Sec. 4.3.1 we keep the hydrodynamic background – consisting of a typical proto-NS configuration – fixed and we only compare the stationary radiation field resulting from the three different aforementioned types of methods. In the second test in Sec. 4.3.2 we then compare the results of a fully dynamic CCSN simulation with two similar calculations performed with well-known Boltzmann-type neutrino-hydrodynamics codes.

4.3.1 Neutrino radiation field of a static proto-neutron star

To compare the different neutrino transport schemes AEF, FLD and Boltzmann with each other in the CCSN context in a manner that is independent of the hydrodynamics part of the numerical method, it is instructive to evolve only the radiation field in a proto-NS background that is held constant during the evolution. As background configurations, we take two profiles of hydrodynamic data obtained from two different simulations performed with the VERTEX code. The hydrodynamic data for our first model (called "pre-explosion model" hereafter) is represented by a snapshot taken at time 150 ms after bounce in the accretion phase of model "N13", which was investigated in the course of Liebendörfer et al.

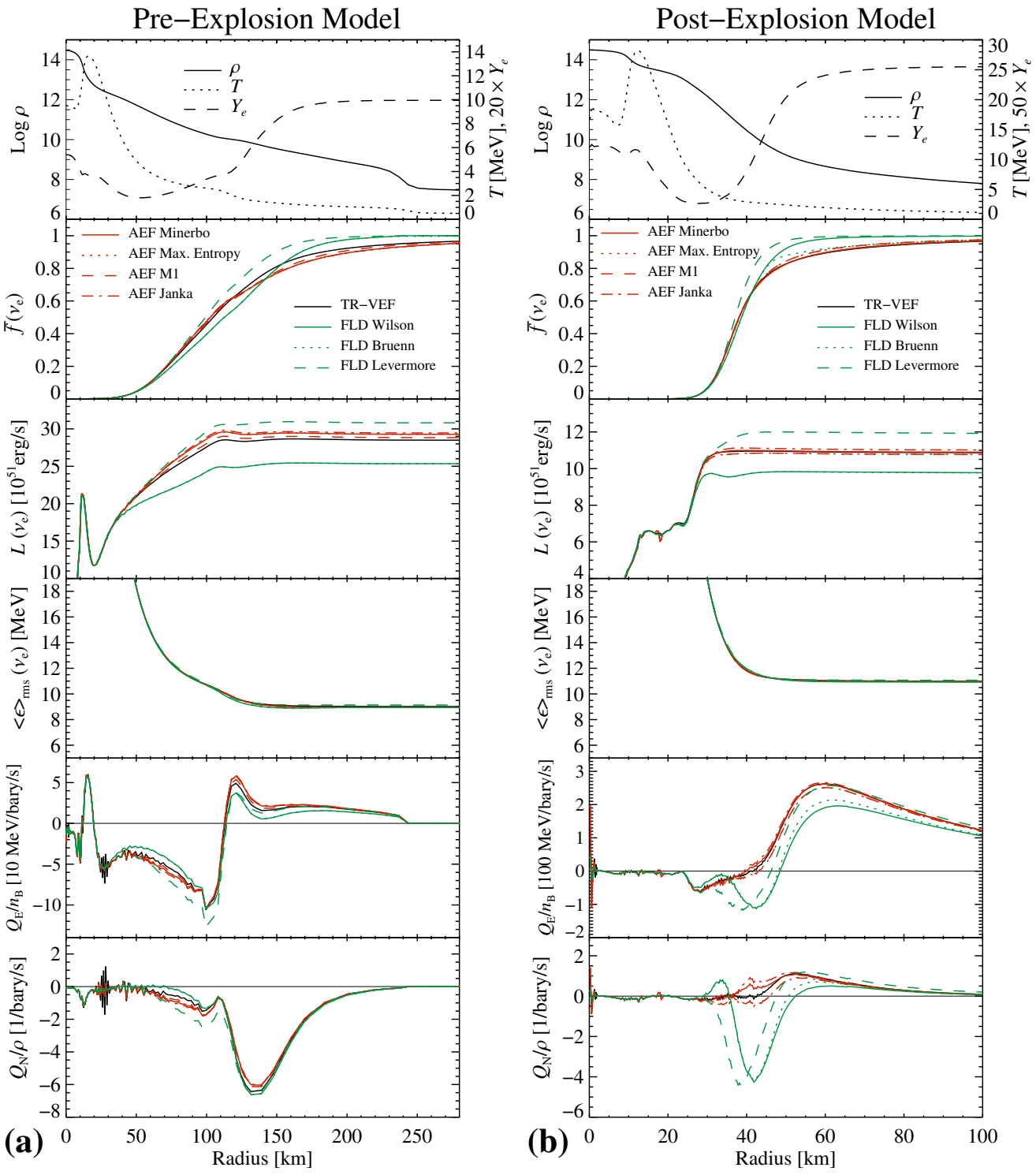

Figure 7. Neutrino radiation field of a static proto-neutron star. We compare for two models (see top title) between different transport schemes (see line labels in the second panel from the top). In the panels are displayed from top to bottom the properties (density ρ, temperature T and electron fraction Y_e) of the hydrodynamic background, the mean flux-factor $\bar{f} \equiv \bar{F}/(c\bar{E})$, luminosity $L \equiv 4\pi r^2 \bar{F}$ and rms-energy $\langle\epsilon\rangle_{\rm rms} \equiv \sqrt{\int \epsilon E(\epsilon)\mathrm{d}\epsilon / \int N(\epsilon)\mathrm{d}\epsilon}$ of electron neutrinos, and the source terms $Q_{\rm E}/n_{\rm B}, Q_{\rm N}/\rho$ for the gas energy density (cf. Eq. (13a)) and electron-number density (cf. Eq. (13c)), respectively. Note that in cases when the dotted green line is invisible it is superimposed by the solid green line.

(2005)[13]. The snapshot for our second model (called "post-explosion model" hereafter) is taken from the model "Sr" in Hüdepohl et al. (2010)[14] in the neutrino-driven wind phase at time 300 ms after core bounce. In both models we adopt the spatial and energy grids and the profiles of the density ρ, temperature T and electron fraction Y_e from the reference calculations, while the remaining quantities needed for the opacities have been obtained by applying the EOS of Lattimer & Swesty (1991). Note that since the data in the pre-explosion model is partially rather noisy we smoothed the original profiles of $\hat{\rho}^0, \hat{T}^0, \hat{Y}_e^0$ as given by the reference calculation by making the replacement $\hat{u}_{\mathsf{i}} = (\hat{u}^0_{\mathsf{i}-1} + 2\hat{u}^0_{\mathsf{i}} + \hat{u}^0_{\mathsf{i}+1})/4$ for $\hat{u} \in \{\hat{\rho}, \hat{T}, \hat{Y}_e\}$ at each radial grid point i in the pre-explosion model. In both models, we ignore frame-dependent effects by setting the velocity $\boldsymbol{v} = 0$ everywhere. Regarding the neutrino interactions, we only take into account the nucleonic β-processes ($n+e^+ \leftrightharpoons p+\bar{\nu}_e$ and $p+e^- \leftrightharpoons n+\nu_e$) and isoenergetic scattering of (anti-)neutrinos off free nucleons as described in Bruenn (1985). Only eletron-type neutrinos are evolved.

For comparison of the AEF scheme with the two remaining schemes, we additionally implemented an FLD scheme and a Boltzmann solver. The FLD scheme was obtained by modifying our existing time-dependent AEF scheme while for the Boltzmann-type solution we implemented a separate algorithm in which the time-independent two-moment system is solved with the closure being provided by a tangent-ray scheme. The details about both methods can be found in Appendix C.

For each of the two background models eight calculations using different methods or closures were performed: The reference solution is represented by the calculation conducted with the Boltzmann-type tangent-ray variable-Eddington-factor scheme (TR-VEF), since this method should yield the most accurate solution. In four additional simulations AEF schemes together with the Eddington factors in Eqs. (28) were employed, while in the remaining three simulations FLD schemes together with the flux-limiters in Eqs. (25) were applied. For computing the flux-limiter $\Lambda_{\mathrm{Bruenn}}$, cf. Eq. (25b), the (energy-dependent) neutrinosphere radii r_ν, defined by

$$\tau_\nu(r_\nu, \epsilon) \equiv \int_{r_\nu}^{\infty} \kappa_{\mathrm{tra}}(r', \epsilon)\mathrm{d}r' = 1\,, \tag{73}$$

were used.

In Fig. 7, we compare for the different calculation methods the radial profiles of the mean flux-factor, luminosity, and rms-energy of electron neutrinos, as well as the hydrodynamic source terms corresponding to heating/cooling and (de-)leptonization resulting from the interaction with both electron neutrinos. We observe the following properties: (1) Concerning the luminosities and flux-factors, the accuracy of the AEF schemes is throughout slightly higher than that of the FLD schemes. While the FLD luminosities and flux factors exhibit errors up to $\sim 10\,\%$, the corresponding AEF quantities are throughout accurate to less than $\sim 3\,\%$. (2) The rms-energies are accurate to $\lesssim 1\,\%$ in all schemes. (3) The accuracy to which the hydrodynamic source terms are reproduced is comparable for AEF and FLD in the pre-explosion model, with the heating rates in the gain region being somewhat underestimated for FLD and overestimated for AEF. In contrast, in the post-explosion model the AEF schemes perform clearly better than the FLD schemes. The main difference between both background models is that the semi-transparent region is more extended in the pre-explosion model. (4) The overall results appear to be more sensitive to different flux-limiters when using FLD than to different Eddington factors when using AEF.

The results of this comparison indicate that AEF methods can perform at least equal to, if not better than, FLD schemes in a 1D proto-NS environment. However, since we have only investigated two stationary snapshots we cannot be sure about the universality of the observed levels of accuracy with respect to time- and model variations. For this reason we avoid at this point to speculate about the hydrodynamic impact of the observed differences in the heating- and deleptonization-rates for the various methods. Nevertheless, the comparison test discussed in the next section demonstrates that AEF schemes can in fact compete with Boltzmann solvers even in the fully dynamic case.

4.3.2 Fully dynamic collapse and post-bounce evolution of a $13\,M_\odot$ progenitor

Our final and most comprehensive test comprises the self-consistent collapse and subsequent post-bounce evolution of the core of a star with approximate main-sequence mass of $13\,M_\odot$ (Nomoto & Mashimoto 1988). This model was already investigated in the comparison in Liebendörfer et al. (2005) (labeled "N13" there) between the neutrino-hydrodynamics codes AGILE-BOLTZTRAN (Liebendörfer et al. 2004) and VERTEX-PROMETHEUS (Rampp & Janka 2002). The comparison revealed a good agreement between the two Boltzmann-type codes, which allows for a straightforward assessment of the accuracy of our method by direct comparison with the results of Liebendörfer et al. (2005)[15]. Note in passing that O'Connor (2014) recently conducted a similar comparison but using the AEF-type code GR1D and inspecting model "G15" from Liebendörfer et al. (2005). The main finding of O'Connor (2014), namely the very good agreement of the AEF scheme with the Boltzmann codes, is in consensus with ours. Finally, using additional, slightly modified simulation setups we will check the robustness of our results with regard to the numerical scheme and the choice of the closure prescription.

4.3.2.1 Model setup We start the spherically symmetric evolution at the onset of collapse when the core has a central density of $\rho_{\mathrm{c}} = 3.16 \times 10^{10}\,\mathrm{g\,cm^{-3}}$ and we follow the system up to a post-bounce time of $t = 300\,\mathrm{ms}$. This test involves all types of neutrino interactions listed in Sec. 2.3. Thus, except for our omission of the processes

[13] See Sec. 4.3.2 for more details about this model, which also served as reference model in the fully dynamic CCSN simulation presented in that section.

[14] The data was provided via http://www.mpa-garching.mpg.de/ccsnarchive/ .

[15] The results discussed in Liebendörfer et al. (2005) and used here as reference data are publically available under http://iopscience.iop.org/0004-637X/620/2/840/fulltext/datafiles.tar.gz

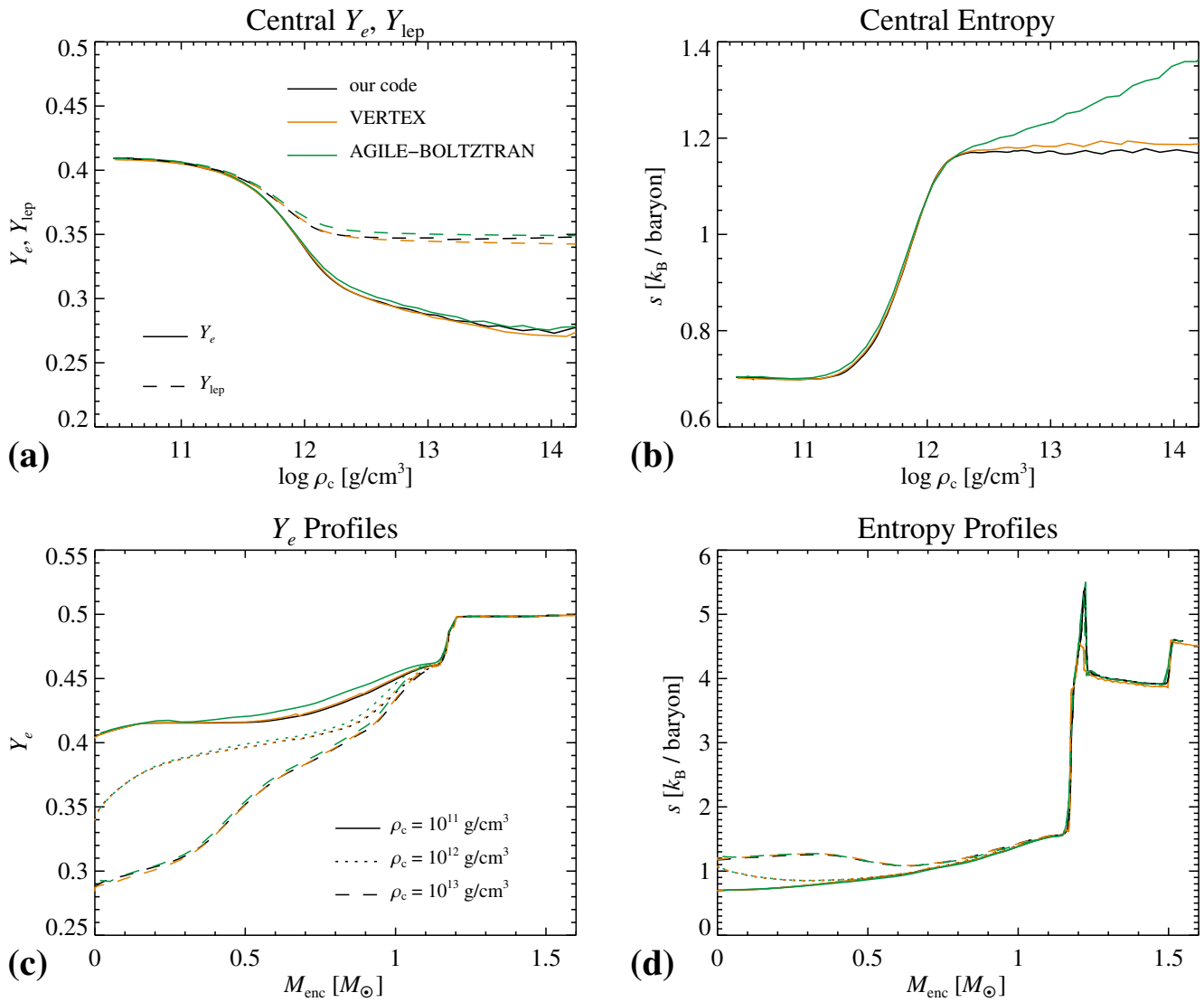

Figure 8. Collapse dynamics in the core-collapse test. All black, orange and green lines display results obtained with our code, VERTEX and AGILE-BOLTZTRAN, respectively. The panels (a) and (b) show the evolution of the central electron (solid lines) and lepton fraction (dashed lines) and the central entropy, respectively, as functions of the central density during collapse. The increase of the central entropy for central densities $\rho_{\rm c} \gtrsim 10^{12}\,{\rm g\,cm^{-3}}$ in the AGILE-BOLTZTRAN run is a numerical artifact which has no impact on the subsequent physical evolution (see Liebendörfer et al. 2005 for more details). The panels (c) and (d) display profiles of the electron fraction and the entropy as functions of the enclosed mass at times when the core reaches the central densities $\rho_{\rm c}$ shown in the legend in panel (c).

$\nu_e\bar{\nu}_e \leftrightharpoons e^-e^+$ [16], we employ the same neutrino microphysics as in Liebendörfer et al. (2005). Above a threshold density of $\rho_{\rm LS} = 6 \times 10^7\,{\rm g\,cm^{-3}}$ the stellar gas is modeled by the nuclear EOS of Lattimer & Swesty (1991), with a compressibility modulus of $K = 180\,{\rm MeV}$. Below this threshold, we use a low-density EOS that includes photons, arbitrarily relativistic and arbitrarily degenerate electrons and positrons, and a non-relativistic Boltzmann gas of baryons. For $\rho > \rho_{\rm LS}$ the nuclear composition is in nuclear statistical equilibrium, which only depends on ρ, T and Y_e. For $\rho < \rho_{\rm LS}$ we assume the baryonic composition to be given by pure ^{28}Si for temperatures $T < 0.44\,{\rm MeV}$, or by pure ^{56}Ni for temperatures $T > 0.44\,{\rm MeV}$.

We employ a Eulerian radial grid with $N_r = 384$ zones distributed logarithmically between the origin and an outer radius of $\approx 7,000\,{\rm km}$ with a minimum grid width of 200 m. The neutrino energy space is discretized into 21 energy bins that are roughly logarithmically distributed between 0 MeV and 400 MeV. For the initialization of the model we take the profiles of velocity, density, electron fraction and entropy from the corresponding AGILE-BOLTZTRAN run. For the time integration of the source terms we ignore the implicit time dependence of the hydrodynamic quantities. Specifically, we use the integration modes *c)* and *b)* described in Sec. 3.6 for densities lower and higher than $10^{11}\,{\rm g\,cm^{-3}}$, respectively. With the CFL factor set to 0.7, our whole simulation required the calculation of about 700,000 time steps.

[16] However, these reactions are subdominant in both the collapse and post-bounce evolution by at least an order of magnitude compared to the dominant reactions, see e.g. Buras et al. 2006.

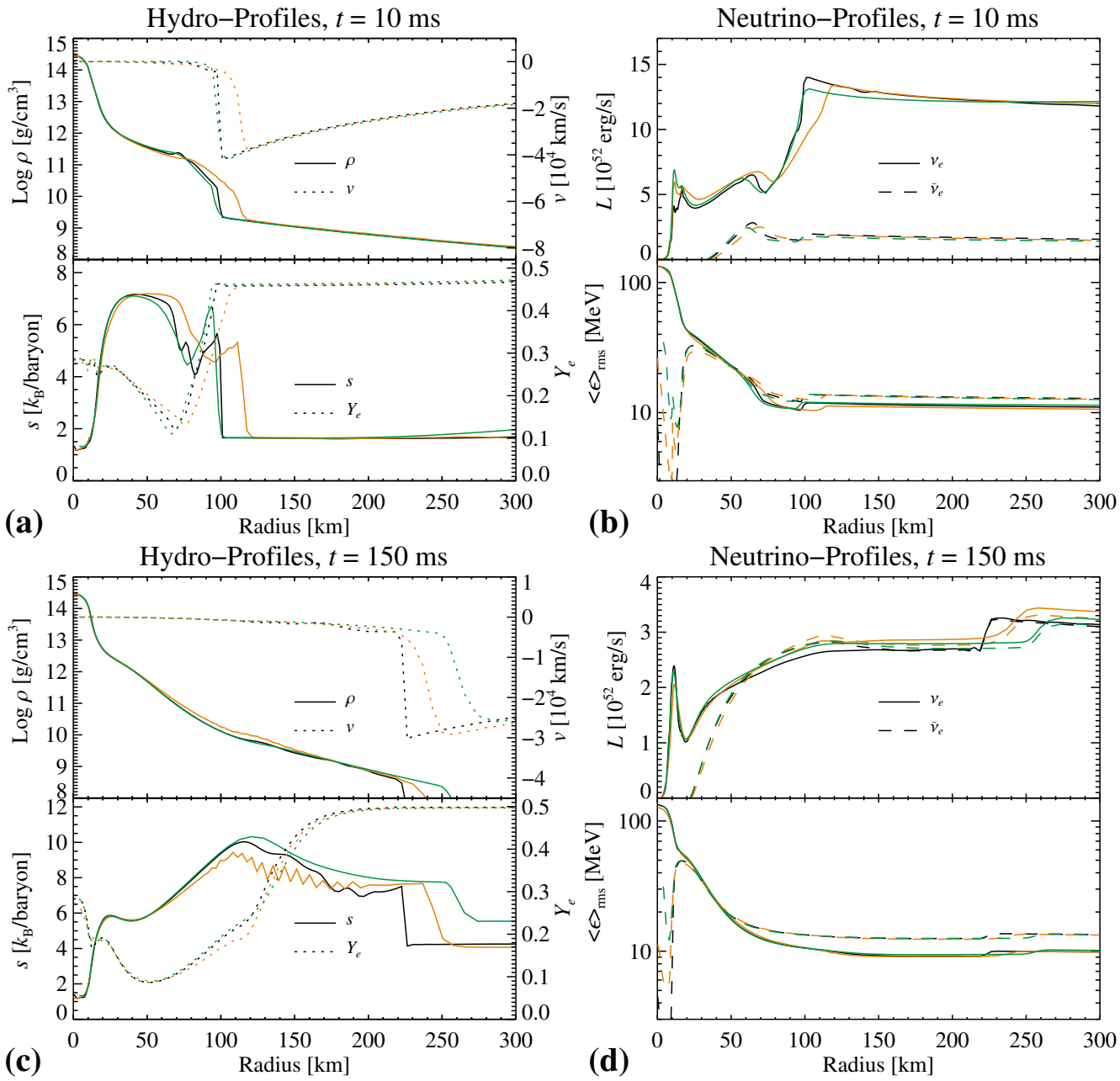

Figure 9. Radial profiles in the post-bounce phase of the core-collapse test. All black, orange and green lines display results obtained with our code, VERTEX and AGILE-BOLTZTRAN, respectively. In panel (a) we show the density and velocity (top), and the entropy per baryon and electron fraction (bottom), while in panel (b) we plot the luminosities (top) and rms-energies (bottom) at a post-bounce time of $t = 10\,\mathrm{ms}$. In panels (c),(d) the same respective quantities as in panels (a),(b) are plotted, but at a post-bounce time of $t = 150\,\mathrm{ms}$.

4.3.2.2 Collapse dynamics The core collapses in a time of $t_{\mathrm{coll}} \simeq 95\,\mathrm{ms}$ to reach a maximum density of $\rho_{\mathrm{max}} = 3.6 \times 10^{14}\,\mathrm{g\,cm^{-3}}$. We show the evolution of the central values of the electron fraction Y_e, lepton fraction $Y_{\mathrm{lep}} \equiv (n_{e^-} - n_{e^+} + \bar{N}_{\nu_e} - \bar{N}_{\bar{\nu}_e})/n_{\mathrm{B}}$ and entropy per baryon s as functions of the central density ρ_{c} during collapse in the top panels and the profiles of Y_e and s as functions of the enclosed mass coordinate $M_{\mathrm{enc}}(r) \equiv 4\pi \int_0^r \rho \tilde{r}^2\,\mathrm{d}\tilde{r}$ in the bottom panels of Fig. 8, respectively. Starting at central densities of about $\rho_{\mathrm{c}} \sim 10^{11}\,\mathrm{g\,cm^{-3}}$, inelastic electron scattering reduces the mean energy of the neutrinos escaping from the core, leading to an accelerated deleptonization and to an increase of the central entropy of the gas. Neutrino trapping sets in at a central density of $\rho_{\mathrm{c}} \approx 2 \times 10^{12}\,\mathrm{g\,cm^{-3}}$, above which the central values of Y_{lep} and s remain roughly constant until core bounce. In all variables, we find a nearly perfect agreement of our results with both reference solutions.

4.3.2.3 Post-bounce evolution Once the core reaches nuclear densities, a shock wave is formed at a mass coordinate of $M_{\mathrm{sh}} \approx 0.67\,M_\odot$, consistent with the reference results. We show the radial profiles of various quantities at two different post-bounce times in Fig. 9 and the time depen-

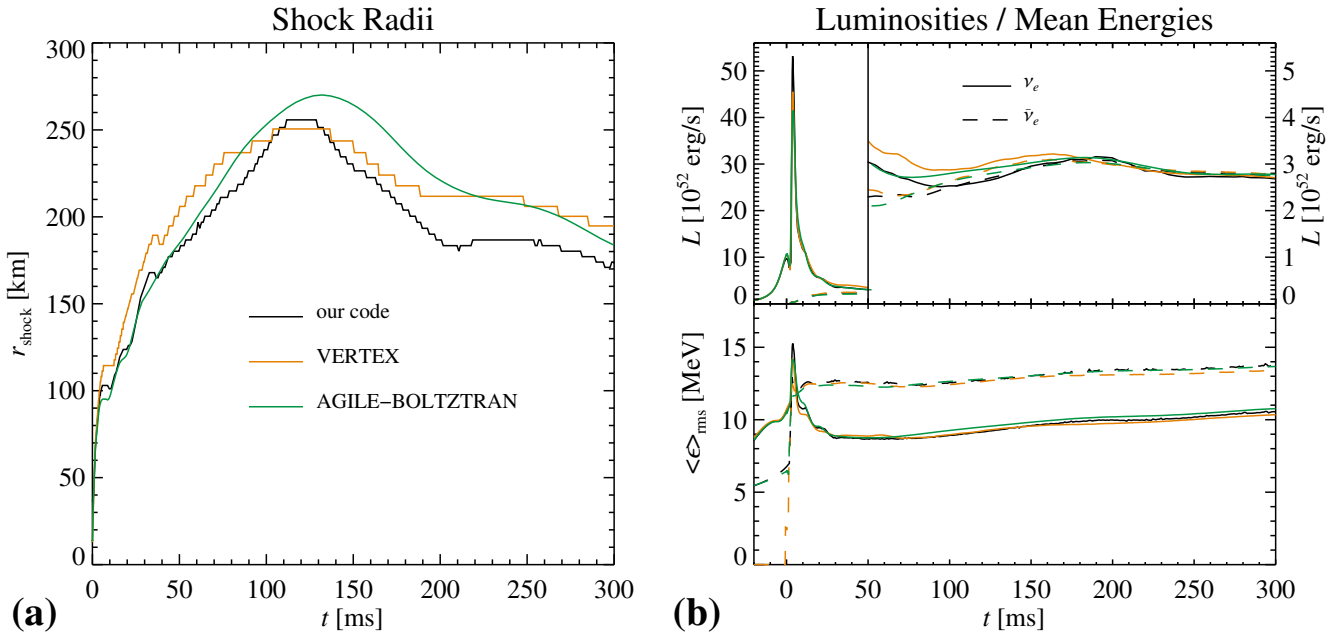

Figure 10. Post-bounce evolution in the core-collapse test. All black, orange and green lines display results obtained with our code, VERTEX and AGILE-BOLTZTRAN, respectively. In panel (a) we show the shock radii as functions of the post-bounce time. The top and bottom of panel (b) depict the luminosities and mean energies, respectively, of electron neutrinos (solid lines) and electron antineutrinos (dashed lines). Note that for the luminosities the scaling on the left y-axis applies for $t < 50\,\mathrm{ms}$, while the scaling on the right y-axis applies for $t > 50\,\mathrm{ms}$.

dence of the shock radius as well as the neutrino luminosities and rms-energies in Fig. 10. All quantities are defined as in Liebendörfer et al. (2005). About $\approx 5\,\mathrm{ms}$ after bounce, the prompt shock reaches a radius of $r_{\mathrm{shock}} \sim 100\,\mathrm{km}$, where it stalls for almost 10 ms. At this point the slightly stronger prompt shock in VERTEX leads to somewhat larger shock radii in the VERTEX runs compared to our simulation and to the AGILE-BOLTZTRAN run. Subsequently, neutrino heating increases the entropy of the matter in the gain region behind the shock and causes the shock to propagate further outward. However, the energy deposition by neutrinos is not sufficient to drive an explosion and we observe a continuous decrease of the shock radius after it has reached its maximum value of $r_{\mathrm{shock}} \approx 250\,\mathrm{km}$ at $t \approx 120\,\mathrm{ms}$. The shock trajectory $r_{\mathrm{shock}}(t)$ (cf. panel (a) of Fig. 10) of our simulation is in good but not perfect agreement with the reference results which, however, are also not exactly consistent with each other. The quantitative differences could to some degree stem from slight differences of the thermodynamic treatment of the low-density regime $\rho < \rho_{\mathrm{LS}}$ to which Liebendörfer et al. (2005) already attributed the discrepancies of $r_{\mathrm{shock}}(t)$ between the two reference models: Differences in the treatment of nuclear burning in the low-density regime lead to different entropies of the material that falls into the shock and thereby to different post-shock entropies. Besides further potentially significant differences in the hydrodynamic treatment of the three codes, the small underestimation of $r_{\mathrm{shock}}(t)$ in our AEF run at late times could also be the result of the approximate closure. However, even though the situation remains unclear, we do not consider this behavior to be very significant, given the fact that even both Boltzmann codes exhibit differences in $r_{\mathrm{shock}}(t)$ of roughly the same size.

4.3.2.4 Neutrino emission At bounce, the core emits a short, intense burst of electron neutrinos. The neutrino burst in our simulation exhibits a higher maximum luminosity of $L_{\mathrm{max}} \approx 5.3 \times 10^{53}\,\mathrm{erg\,s^{-1}}$ than in the two reference solutions ($L_{\mathrm{max}} \approx 4.14 \times 10^{53}\,\mathrm{erg\,s^{-1}}$ and $L_{\mathrm{max}} \approx 4.55 \times 10^{53}\,\mathrm{erg\,s^{-1}}$ for AGILE-BOLTZTRAN and VERTEX, respectively). However, the shorter duration of the burst in our model compensates for this, and the integrated energy emitted during the burst, $E_{\mathrm{burst}} \equiv \int_0^{0.02\,\mathrm{s}} L_{\nu_e}(t)\,\mathrm{d}t$, is almost equal for all three codes: $E_{\mathrm{burst}} = 2.80$, 2.80, and $2.85 \times 10^{51}\mathrm{erg}$ for our model, AGILE-BOLTZTRAN, and VERTEX, respectively. The reason for our neutrino burst being sharper may be found in the numerical treatment: Our explicit time integration (at least for the hyperbolic terms which describe the propagation of radiation) combined with a high-order spatial discretization is certainly less dissipative than both fully-implicit reference schemes, which facilitates the accurate evolution of narrow radiation peaks. Note that this explanation is supported by the fact that O'Connor (2014) obtain a similarly enhanced neutrino burst using their explicit AEF scheme; see their Fig. 6.

After the end of the neutrino burst, the luminosity of electron neutrinos drops quickly while the luminosity of electron antineutrinos increases, and subsequently neutrinos of both flavors are emitted at about equal luminosities. After the mean energies of both flavors peak at the neutrino burst they remain approximately constant with a slow trend towards higher values. Due to their larger interaction rates with matter, electron neutrinos decouple at lower densities and temperatures than electron antineutrinos, leading to a mean energy that is $\sim 3\,\mathrm{MeV}$ below that of the antineutrinos.

In summary, most of our results lie well within the tol-

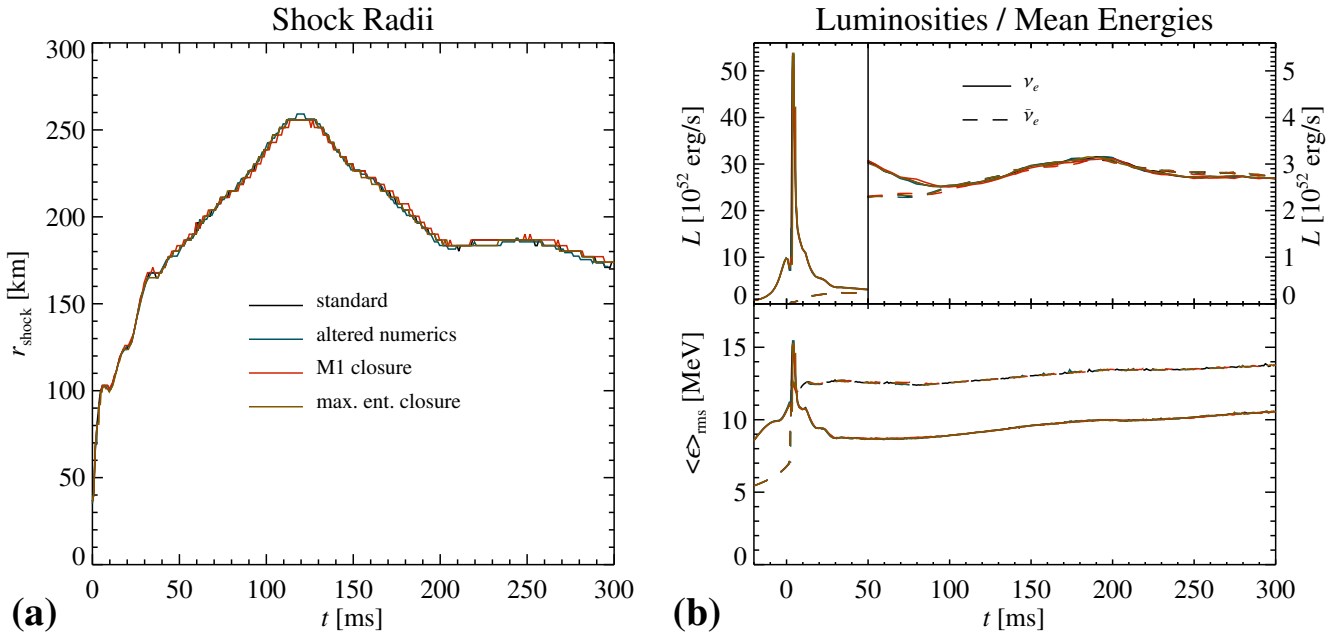

Figure 11. Same as Fig. 10 but for the runs "standard", "altered numerics", "M_1 closure", and "maximum entropy closure" described in text. The maxima of the neutrino bursts in these models are $L_{\max} \approx \{5.3, 5.3, 5.1, 5.4\} \times 10^{53}\,\mathrm{erg\,s^{-1}}$, respectively.

erance region spanned by the results of both reference calculations, such that no obvious deficiencies of the AEF method can be identified.

4.3.2.5 Variations of the calculation method In this last study, we address various issues to check the robustness of the results presented above and therefore the reliability of the whole algorithm described in this paper. To this end, we perform additional test runs that are described below. In what follows, we denote the simulation presented above as the "standard" run. In Fig. 11 we show similar quantities as in Fig. 10 but we compare the "standard" run with the test runs described below.

We set up a simulation identical to the "standard" run described above but with altered numerical specifications, called "altered numerics". The number of spatial grid points is increased to 576 (with an unchanged innermost grid width of 200 m) and the time step is reduced according to CFL=0.3. Moreover, the integration mode for the source terms *a)* is used instead of *b)* for densities $\rho > 10^{11}\,\mathrm{g\,cm^{-3}}$ (cf. Sec. 3.6). As a final difference to the "standard" run, we additionally take into account all the velocity-/acceleration-dependent terms that have been dropped when deriving the moment equations, Eqs. (7), from the transfer equation, Eq. (4), in Sec. 2. For the numerical implementation of these terms we adopt methods in close analogy to the existing ones, cf. Sec. 3. This model yields very similar results compared to the standard case, as is exemplarily shown for selected functions of time in Fig. 11. This similarity between the two models proves the robustness of our integration method regarding several aspects, at least for physical conditions similar to the investigated case of a one-dimensional CCSN: Besides convergence regarding the spatial resolution the test evinces that the mixed explicit–implicit time-integration scheme does not produce time-step dependent numerical artefacts. Furthermore, the test justifies the time-explicit treatment of the hydrodynamic quantities in the source-term integration. Finally, the test verifies that the velocity-dependent terms dropped in Eqs. (7) are truly insignificant.

Two additional calculations with different closure prescriptions are conducted: In one run, "M_1 closure", the closure in Eq. (28b) and in the other run, "maximum entropy closure", the closure in Eq. (28d) is used to express the Eddington factor χ. For simplicity, we keep using the Minerbo prescription for the 3rd-moment factors q, cf. Eq. (33). Since the 3rd-moment terms are of minor relevance compared to the terms including the 2nd moments (recall that the 3rd-moment terms vanish in the energy-integrated 1st-moment equation) this is a justified approximation to test the dominant impact of using a different closure prescription. All three simulations that make use of different closures give almost identical results, as is shown in Fig. 11 for selected quantities. This important result is consistent with the findings in Sec. 4.3.1 and it suggests that the AEF algorithm is sufficiently self-consistent when applied to CCSNe, in the sense that the outcome of the calculation is rather insensitive to the precise shape of the closure.

5 SUMMARY

We presented the neutrino-transport code ALCAR that was developed to perform multidimensional simulations of CCSNe and (different stages of) NS-mergers. The energy-dependent neutrino-transport scheme is based on the multi-group evolution (with full energy-bin coupling) of the first two angular moments of the specific intensity defined in the frame comoving with the fluid, and it takes into account the dominant $\mathcal{O}(v/c)$ terms describing fluid-advection, aberration and Doppler shift. The resulting system of equations

for the neutrino energy density and the three components of the flux density (cf. Eqs. (7)) is closed by an approximate prescription for the Eddington tensor, which assumes that the specific intensity is axisymmetric around the direction of the flux-density vector and that the remaining single parameter χ is given by an algebraic function of the evolved radiation moments (cf. Eqs. (28)). Thereby, the resulting AEF method circumvents the computationally demanding task to solve for the detailed angular dependence of the specific intensity as it is done in Boltzmann-solvers. In contrast to the standard FLD method, the AEF method consistently evolves the 1st moments and, hence, it is potentially more accurate (see, e.g., the test in Sec. 4.3.1), it allows radiation anisotropies to be described (cf. Sec. 4.2.1), and it ensures the conservation of the total (radiation plus fluid) momentum and energy up to $\mathcal{O}(v/c)$ (Baron et al. 1989; Cernohorsky & van den Horn 1990). Finally, a computationally relevant difference between the AEF and FLD methods is that the time step in the case of a time-explicit advection scheme is required to be considerably smaller in the FLD than in the AEF formulation, in practice forcing realizations of the former method to employ fully implicit time-integration algorithms (cf. Sec. 2.4).

Our numerical scheme essentially follows the ideas presented in Pons et al. (2000) and Audit et al. (2002), which have recently been implemented also in a number of photon-transport (e.g. Hayes & Norman 2003; Aubert & Teyssier 2008; Sądowski et al. 2013; Skinner & Ostriker 2013; McKinney et al. 2014) and neutrino-transport (Shibata & Sekiguchi 2012; Takahashi et al. 2013; O'Connor 2014) codes. The basic strategy is to utilize the hyperbolic nature of the moment equations to employ a Godunov-type scheme, in which the advection fluxes between grid cells are given as solutions of Riemann problems. Thanks to a neutrino-number conservative scheme developed by Müller et al. (2010) to handle the Doppler shift terms we avoid the simultaneous evolution of the number-related moments together with the energy-based moments. A distinctive feature of the presented scheme compared to existing FLD and most Boltzmann-type neutrino-transport solvers is that all except the source terms are integrated explicitly in time. Although in this case the time step resulting from the Courant condition is comparable to the light-crossing times of single grid cells, it will usually only be marginally (or at least not several orders of magnitude) lower than the already small fluid time steps in the hot and dense physical systems this code is supposed to be applied to. To capture the transition to the stiff parabolic limit of the moment equations in a numerically consistent and stable fashion, the source terms are handled time-implicitly and the upwind-type Riemann solver switches to a central-type solver in optically thick regions. Since the implicitly handled source terms are only functions of the local neutrino-gas properties, a computationally convenient feature of this explicit–implicit integration scheme is that the method can be parallelized with high efficiency.

We conducted a series of tests to assess the quality of the AEF method and to check the correct implementation of the velocity-dependent terms, the source terms and the coupling to the hydrodynamics part of the code. By means of one- and two-dimensional test problems it was shown that the AEF method allows for a stable and self-consistent evolution of the radiation field in the full range between isotropic diffusion and free-streaming, including the accurate description of frame-dependent effects such as Doppler shift and diffusion in static and moving media. Although this was done here in two dimensions, the code readily generalizes to three dimensions.

Two additional tests specifically focused on (one-dimensional) neutrino transport in CCSNe. In the first test the hydrodynamic background, consisting of a proto-NS configuration, was held fixed to compare the neutrino fields resulting from an AEF scheme with different Eddington factors with the outcomes of an FLD scheme with different flux-limiters and of a more accurate Boltzmann scheme. The essential findings were that the AEF solvers reproduced the results of the Boltzmann solver slightly more accurately than the FLD scheme and that using different closure prescriptions has less impact on the solution in an AEF scheme than in an FLD scheme. In the last test we performed a fully dynamic core-collapse simulation up to 300 ms post bounce and we found very good agreement with the corresponding results obtained with the Boltzmann-type RHD codes VERTEX-PROMETHEUS and AGILE-BOLTZTRAN. For this scenario we conducted additional test runs which checked the robustness with respect to our integration algorithm and that revealed the convenient outcome that the physical results only marginally depend on the actual choice of the closure relation.

Although in this paper we investigated many cases in which the AEF method yields results comparable to the Boltzmann equation, one should keep in mind that the computational advantages of the AEF method compared to a Boltzmann solver do not come for free. That is, the closure relation between angular moments cannot be fulfilled to the same degree for arbitrarily complex radiation fields. A related, particular shortcoming of the AEF method is that even in the optically thin limit radiation fronts interfere with each other, which is an immediate result of the closure being a generally non-linear function of the evolved moments (for consequences of this features in the case of a post-merger BH-torus system, see the appendix of Just et al. 2015). Nevertheless, we consider these deficiencies to be not overly restrictive for our purposes since the present code is primarily designed to describe systems in which a single extended source dominantly determines the evolution of the radiation field.

We have already started to operate the described code to examine the combined neutrino- and magnetic-field effects in two-dimensional CCSNe (Obergaulinger et al. 2014) and to study the impact of neutrino transport on outflows from post-NS merger BH-accretion tori (Just et al. 2015). Since here we only discussed test problems which are simplified in one way or another we refer the reader to these mentioned papers for more specific discussions of results obtained with the AEF scheme in multidimensional applications. In the future we plan to improve the presented code by supplementing the coevolution of μ- and τ-neutrinos, refining the set of neutrino-interaction channels, and adding relativistic corrections.

ACKNOWLEDGMENTS

We are grateful to Bernhard Müller for helpful discussions about various neutrino-transport issues, to Lorenz Hüdepohl for providing his VERTEX-PROMETHEUS data used for the test in Sec. 4.3.1, to Bruno Peres for useful comments, and to the anonymous referee for helping to improve the clarity of the manuscript. We acknowledge support by the Max-Planck/Princeton Center for Plasma Physics (MPPC), by the Deutsche Forschungsgemeinschaft through the Transregional Collaborative Research Center SFB/TR 7 "Gravitational Wave Astronomy", by the Computational Center for Particle and Astrophysics (C2PAP) as part of the Cluster of Excellence EXC 153 "Origin and Structure of the Universe", by the European Research Council through ERC-AdG No. 341157-COCO2CASA at Garching and grant CAMAP-259276 at Valencia, and by the Spanish Ministerio de Ciencia e Innovación through grant AYA2013-40979-P Astrofísica Relativista Computacional at Valencia. The computations were performed at the Rechenzentrum Garching, the Leibniz-Rechenzentrum, and at the cluster Lluisvives of the University of Valencia.

REFERENCES

Ascher U. M., Ruuth S. J., Spiteri R. J., 1997, Applied Numerical Mathematics, 25, 151
Aubert D., Teyssier R., 2008, MNRAS, 387, 295
Audit E., Charrier P., Chièze J. ., Dubroca B., 2002, preprint (arXiv:astro-ph/0206281)
Baron E., Myra E. S., Cooperstein J., van den Horn L. J., 1989, ApJ, 339, 978
Bludman S. A., Cernohorsky J., 1995, Phys. Rep., 256, 37
Bruenn S. W., 1985, ApJS, 58, 771
Buchler J. R., 1979, Journal of Quantitative Spectroscopy and Radiative Transfer, 22, 293
Buras R., Rampp M., Janka H.-T., Kifonidis K., 2006, A&A, 447, 1049
Burrows A., 2013, Reviews of Modern Physics, 85, 245
Cardall C. Y., Endeve E., Mezzacappa A., 2013, Phys. Rev. D, 87, 103004
Cernohorsky J., Bludman S. A., 1994, ApJ, 433, 250
Cernohorsky J., van Weert C. G., 1992, ApJ, 398, 190
Cernohorsky J., van den Horn L. J., 1990, J. Quant. Spec. Radiat. Transf., 43, 33
Cernohorsky J., van den Horn L. J., Cooperstein J., 1989, J. Quant. Spec. Radiat. Transf., 42, 603
Dessart L., Ott C. D., Burrows A., Rosswog S., Livne E., 2009, ApJ, 690, 1681
Dgani R., Cernohorsky J., 1991, J. Quant. Spec. Radiat. Transf., 46, 1
Dgani R., Janka H.-T., 1992, A&A, 256, 428
Dubroca B., Feugeas J., 1999, Academie des Sciences Paris Comptes Rendus Serie Sciences Mathematiques, 329, 915
Ensman L., 1994, ApJ, 424, 275
Fernández R., Metzger B. D., 2013, MNRAS, 435, 502
Godunov S., 1959, Mat. Sb. (N.S.), 47(89), 271
González M., Audit E., Huynh P., 2007, A&A, 464, 429
Hanke F., Marek A., Müller B., Janka H.-T., 2012, ApJ, 755, 138
Harten A., Lax P. D., van Leer B., 1983, Siam Review, 25
Hayes J. C., Norman M. L., 2003, ApJS, 147, 197
Hubeny I., Burrows A., 2007, ApJ, 659, 1458
Hüdepohl L., Müller B., Janka H., Marek A., Raffelt G. G., 2010, Physical Review Letters, 104, 251101
Iliev I. T., et al., 2006, MNRAS, 371, 1057
Janka H.-T., 1991, PhD thesis, , Technische Universität München, (1991)
Janka H.-T., 2012, Annual Review of Nuclear and Particle Science, 62, 407
Jiang Y.-F., Stone J. M., Davis S. W., 2012, ApJS, 199, 14
Just O., Bauswein A., Pulpillo R. A., Goriely S., Janka H.-T., 2015, MNRAS, 448, 541
Kaneko N., Morita K., Maekawa M., 1984, Ap&SS, 107, 333
Koerner A., Janka H.-T., 1992, A&A, 266, 613
Kuroda T., Kotake K., Takiwaki T., 2012, ApJ, 755, 11
Kuroda T., Takiwaki T., Kotake K., 2014, Phys. Rev. D, 89, 044011
Lattimer J. M., Swesty F., 1991, Nuclear Physics A, 535, 331
Levermore C. D., 1984, Journal of Quantitative Spectroscopy and Radiative Transfer, 31, 149
Levermore C. D., Pomraning G. C., 1981, ApJ, 248, 321
Liebendörfer M., Messer O. E. B., Mezzacappa A., Bruenn S. W., Cardall C. Y., Thielemann F.-K., 2004, ApJS, 150, 263
Liebendörfer M., Rampp M., Janka H., Mezzacappa A., 2005, ApJ, 620, 840
Liebendörfer M., Whitehouse S. C., Fischer T., 2009, ApJ, 698, 1174
Liu X.-D., Osher S., Chan T., 1994, Journal of Computational Physics, 115, 200
Livne E., Burrows A., Walder R., Lichtenstadt I., Thompson T. A., 2004, ApJ, 609, 277
Lowrie R. B., Mihalas D., Morel J. E., 2001, Journal of Quantitative Spectroscopy and Radiative Transfer, 69, 291
McKinney J. C., Tchekhovskoy A., Sadowski A., Narayan R., 2014, MNRAS, 441, 3177
Mihalas D., 1980, ApJ, 237, 574
Mihalas D., Mihalas B. W., 1984, Foundations of radiation hydrodynamics. New York, Oxford University Press
Minerbo G. N., 1978, J. Quant. Spec. Radiat. Transf., 20, 541
Müller B., Janka H.-T., Dimmelmeier H., 2010, ApJS, 189, 104
Munier A., Weaver R., 1986, Computer Physics Reports, 3, 165
Nomoto K., Mashimoto M., 1988, Phys. Rep., 163, 13
O'Connor E., 2014, preprint (arXiv:1411.7058)
O'Connor E., Ott C. D., 2013, ApJ, 762, 126
Obergaulinger M., 2008, PhD thesis, Technical University Munich
Obergaulinger M., Janka H.-T., Aloy M. A., 2014, MNRAS, 445, 3169
Ott C. D., Burrows A., Dessart L., Livne E., 2008, ApJ, 685, 1069
Pareschi L., Russo G., 2005, Journal of Scientific Computing, 25, 129
Pennisi S., 1992, International Journal of Engineering Science, 30, 679
Pennisi S., Trovato M., 1987, International Journal of En-

gineering Science, 25, 1059
Plewa T., Müller E., 1999, A&A, 342, 179
Pons J. A., Ibáñez J. M., Miralles J. A., 2000, MNRAS, 317, 550
Popham R., Woosley S. E., Fryer C., 1999, ApJ, 518, 356
Qian Y., Woosley S. E., 1996, ApJ, 471, 331
Rampp M., Janka H., 2002, A&A, 396, 361
Sądowski A., Narayan R., Tchekhovskoy A., Zhu Y., 2013, MNRAS, 429, 3533
Schinder P. J., Bludman S. A., 1989, ApJ, 346, 350
Shibata M., Sekiguchi Y., 2012, Progress of Theoretical Physics, 127, 535
Shibata M., Kiuchi K., Sekiguchi Y., Suwa Y., 2011, Progress of Theoretical Physics, 125, 1255
Sincell M. W., Gehmeyr M., Mihalas D., 1999, Shock Waves, 9, 391
Skinner M. A., Ostriker E. C., 2013, ApJS, 206, 21
Smit J. M., Cernohorsky J., Dullemond C. P., 1997, Astronomy and Astrophysics
Smit J. M., van den Horn L. J., Bludman S. A., 2000, A&A, 356, 559
Sumiyoshi K., Takiwaki T., Matsufuru H., Yamada S., 2015, ApJS, 216, 5
Suresh A., Huynh H. T., 1997, Journal of Computational Physics, 136, 83
Swesty F. D., Myra E. S., 2009, ApJS, 181, 1
Takahashi H. R., Ohsuga K., Sekiguchi Y., Inoue T., Tomida K., 2013, ApJ, 764, 122
Toro E., 1997, Riemann solvers and numerical methods for fluid dynamics: a practical introduction. Springer Verlag
Turner N. J., Stone J. M., 2001, ApJS, 135, 95
Vaytet N. M. H., Audit E., Dubroca B., Delahaye F., 2011, J. Quant. Spec. Radiat. Transf., 112, 1323
Wanajo S., Janka H.-T., 2012, ApJ, 746, 180
Wilson J. R., Couch R., Cochran S., Le Blanc J., Barkat Z., 1975, in Bergman P. G., Fenyves E. J., Motz L., eds, Annals of the New York Academy of Sciences Vol. 262, Seventh Texas Symposium on Relativistic Astrophysics. pp 54–64, doi:10.1111/j.1749-6632.1975.tb31420.x
Yorke H. W., 1980, A&A, 86, 286
Zeldovich Y. B., Raizer Y. P., 1966, Elements of gasdynamics and the classical theory of shock waves. New York: Academic Press

APPENDIX A: DERIVATION OF THE 3RD-MOMENT FACTOR FOR THE MINERBO CLOSURE

Here we outline the derivation of Eq. (33), which expresses the 3rd-moment factor q as a function of the flux factor f assuming that the radiation field obeys the Minerbo closure. The Minerbo closure can be found by maximizing the entropy functional for a particle configuration with a low number density (Minerbo 1978; see also Cernohorsky & Bludman 1994). This leads to the axisymmetric distribution function

$$\mathcal{F}(\mu) = \frac{1}{4\pi}\mathrm{e}^{a\mu-\eta}\,, \tag{A1}$$

in which μ is the cosine of the angle between the direction of particle momentum and the symmetry axis, and the parameters a, η are two Lagrange multipliers. The latter can be eliminated using the definition of the 0th and 1st moments (cf. Eq. (5)),

$$E = \left(\frac{\epsilon}{hc}\right)^3 \int \mathrm{d}\Omega\mathcal{F} = \left(\frac{\epsilon}{hc}\right)^3 \frac{\mathrm{e}^{-\eta}}{a}\sinh a\,, \tag{A2a}$$

$$\frac{1}{c}F = \left(\frac{\epsilon}{hc}\right)^3 \int \mathrm{d}\Omega\mu\mathcal{F} = \left(\frac{\epsilon}{hc}\right)^3 \frac{\mathrm{e}^{-\eta}}{a}\left(\cosh a - \frac{\sinh a}{a}\right)\,, \tag{A2b}$$

which results in

$$f \equiv \frac{F}{cE} = \coth a - \frac{1}{a} = L(a) \tag{A3}$$

and, hence, in $a = L^{-1}(f)$, where L and L^{-1} are the Langevin function and its inverse, respectively. Since L cannot be inverted analytically, we employ for all practical purposes the following approximation of L^{-1} Cernohorsky & Bludman (1994):

$$a = L^{-1}(f) \approx \frac{15f}{5 - 3f^2 + f^3 - 3f^4}\,, \tag{A4}$$

of which the error is at most a few per cent. Now, the 2nd-moment factor χ, Eq. (28a), and 3rd-moment factor q, Eq. (33), are obtained from their definition in Eqs. (29) and (31), respectively, using Eqs. (A1)–(A4) and $\boldsymbol{n}\cdot\boldsymbol{n}_{\boldsymbol{F}} = \mu$.

APPENDIX B: MULTIDIMENSIONAL CHARACTERISTIC WAVE SPEEDS

In this section we provide supplementary information about the speeds $\lambda_{\pm,0}$ (cf. Sec. 3.4) of the characteristic waves associated with the hyperbolic part of the multidimensional two-moment system closed by an algebraic Eddington tensor. Without loss of generality, we consider characteristic waves propagating along the x-direction and assume that the 1st-moment vector $\boldsymbol{F} = (F_x, F_y) = (\mu, \sqrt{1-\mu^2})|\boldsymbol{F}|$ lies in the $x-y$ plane and forms an angle $\alpha_{\boldsymbol{F}}$, where $\mu \equiv \cos\alpha_{\boldsymbol{F}}$, with the x-axis. The wave speeds are then obtained as eigenvalues of the Jacobi matrix whose components are given in terms of a general closure $\chi(e, f)$ as follows:

$$\left(\frac{\partial F_x}{\partial E}, \frac{\partial F_x}{\partial F_x}, \frac{\partial F_x}{\partial F_y}\right) = \big(0, 1, 0\big)\,, \tag{B1a}$$

$$c^2\frac{\partial P_{xx}}{\partial E} = \frac{c^2}{2}\left[1 - \mu^2 + (3\mu^2 - 1)\left(e\frac{\partial\chi}{\partial e} - f\frac{\partial\chi}{\partial f} + \chi\right)\right]\,, \tag{B1b}$$

$$c^2\frac{\partial P_{xx}}{\partial F_x} = \frac{c\mu}{2f}\left[f\frac{\partial\chi}{\partial f}\left(3\mu^2 - 1\right) - 2(\mu^2 - 1)(3\chi - 1)\right]\,, \tag{B1c}$$

$$c^2\frac{\partial P_{xx}}{\partial F_y} = \frac{c\sqrt{1-\mu^2}}{2f}\left[f\frac{\partial\chi}{\partial f}(3\mu^2 - 1) - 2\mu^2(3\chi - 1)\right]\,, \tag{B1d}$$

$$c^2\frac{\partial P_{xy}}{\partial E} = \frac{c^2\mu\sqrt{1-\mu^2}}{2}\left[3\left(e\frac{\partial\chi}{\partial e} - f\frac{\partial\chi}{\partial f} + \chi\right) - 1\right]\,, \tag{B1e}$$

$$c^2\frac{\partial P_{xy}}{\partial F_x} = \frac{c\sqrt{1-\mu^2}}{2f}\left[3\chi - 1 + \mu^2\left(2 + 3f\frac{\partial\chi}{\partial f} - 6\chi\right)\right]\,, \tag{B1f}$$

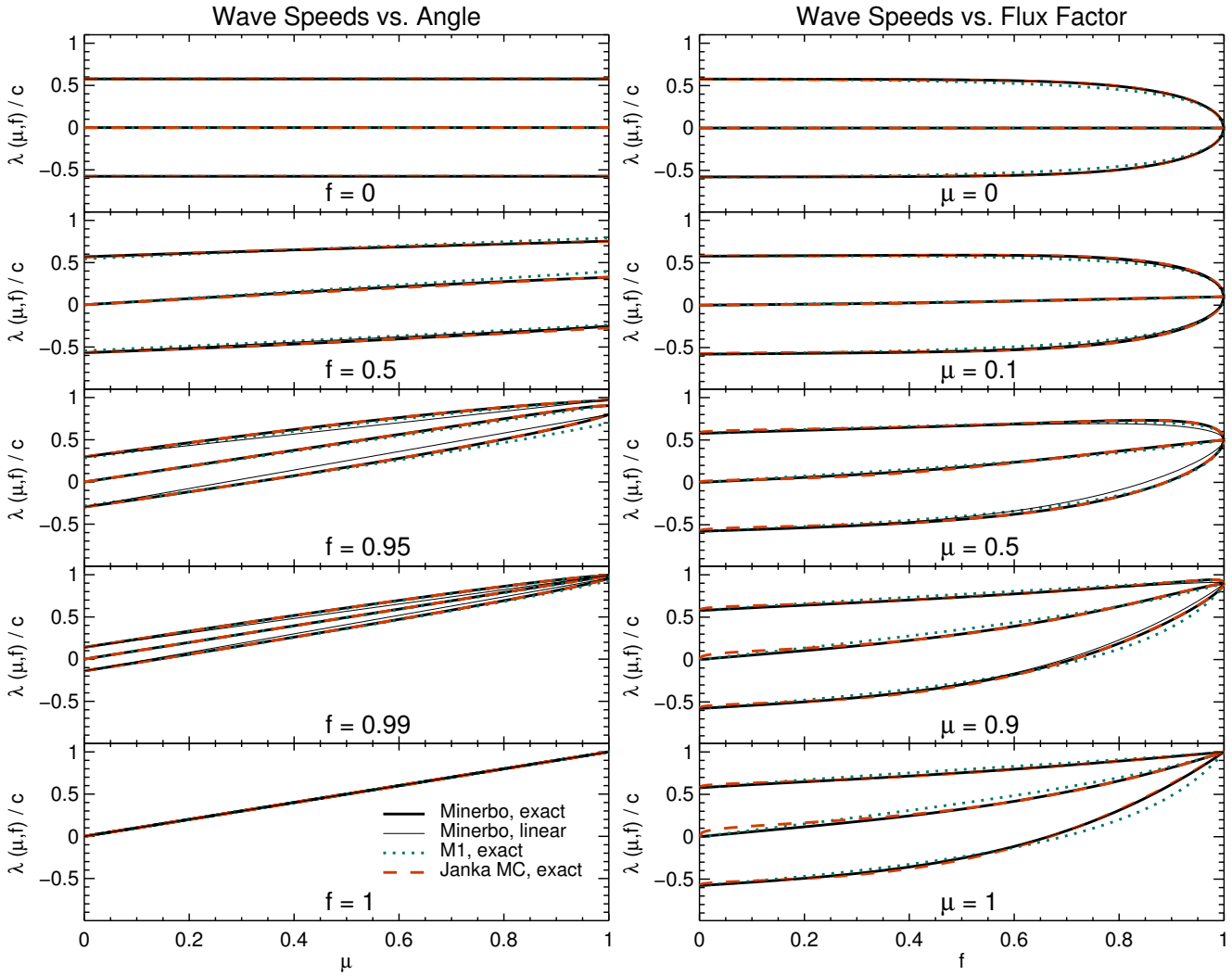

Figure B1. Comparison of characteristic speeds $\lambda_{\pm,0}(\mu, f)$ (with $\lambda_- < \lambda_0 < \lambda_+$) as functions of the direction cosine μ (left) and flux factor f (right) for the Minerbo, M_1 and Monte-Carlo closure (cf. $\chi_{\rm Minerbo}, \chi_{M_1}$ and $\chi_{\rm Janka}$ in Eqs. (28), respectively). The thick lines denote the exact wave speeds while the thin black lines depict for the Minerbo closure the linear expansion in μ, cf. Eq. (46).

$$c^2 \frac{\partial P_{xy}}{\partial F_y} = \frac{c\mu}{2f}\left[3f\frac{\partial \chi}{\partial f}(1-\mu^2) + (2\mu^2-1)(3\chi-1)\right] . \tag{B1g}$$

We plot in Fig. B1 the resulting wave speeds as functions of μ and f for three different closures together with the linear expansion in μ, Eq. (46), for the Minerbo closure. It can be seen that all considered closures lead to rather similar wave speeds. Moreover, the μ-dependence of the wave speeds is very close to linear, which suggests that using the linearized versions instead of the exact wave speeds as signal speeds for the Riemann solver, cf. Eq. (48), is a justified approximation.

APPENDIX C: NUMERICAL METHODS USED FOR THE COMPARISON IN SEC. 4.3.1

C1 Flux-limited diffusion solver

To construct the spherically symmetric FLD solver used to find the corresponding solutions in Sec. 4.3.1 we start from the presented AEF scheme and essentially drop the evolution equation for the radial flux density $F_r = F$ and all velocity-dependent terms. What remains to be determined is a suitable numerical representation of the flux $F_{\rm FLD}$ (cf. Eq. (22)) at each cell interface. To this end, we first compute the cell-centered version of the flux, for which we need a cell-centered representation of $\partial_r E$. The latter is discretized as

$$\partial_r E \longrightarrow (\hat{E}_{\mathsf{i}+1} - \hat{E}_{\mathsf{i}-1})/(2\Delta r_{\mathsf{i}}) , \tag{C1}$$

where i denotes the radial grid index and $\Delta r_{\mathsf{i}} \equiv r_{\mathsf{i}+\frac{1}{2}} - r_{\mathsf{i}-\frac{1}{2}}$. Out of the resulting cell-centered values $\hat{F}_{{\rm FLD},\mathsf{i}}$ of the flux density, we compute the cell-interface values as

$$\hat{F}_{{\rm FLD},\mathsf{i}+\frac{1}{2}} \equiv \lambda_{{\rm FLD},\mathsf{i}+\frac{1}{2}} \hat{F}_{{\rm FLD},\mathsf{i}} + (1-\lambda_{{\rm FLD},\mathsf{i}+\frac{1}{2}})\hat{F}_{{\rm FLD},\mathsf{i}+1} , \tag{C2}$$

where the interpolation parameter $\lambda_{\rm FLD} \in [0,1]$ is introduced to ensure that the numerical method is based on central-type fluxes in the parabolic regime, where $\lambda_{\rm FLD} \to 1/2$ should hold, and on upwind-type fluxes in the hyperbolic regime, where $\lambda_{\rm FLD} \to 1$ for $f \equiv F_{\rm FLD}/(cE) \to 1$

and $\lambda_{\rm FLD} \to 0$ for $f \to -1$ should hold. We compute $\lambda_{\rm FLD}$ as a function of the signed, average flux-factor $f_{\mathsf{i}+\frac{1}{2}} \equiv (\hat{F}_{\rm FLD,i}/\hat{E}_{\mathsf{i}} + \hat{F}_{\rm FLD,i+1}/\hat{E}_{\mathsf{i}+1})/(2c)$ as

$$\lambda_{\rm FLD,i+\frac{1}{2}} \equiv \max\{\, \min\{\, f_{\mathsf{i}+\frac{1}{2}} + 1/2, 1\},\, 0\}\,. \tag{C3}$$

The time step Δt for the explicit integration is chosen to fulfill $\Delta t < \min_{\mathsf{i}}\{\tau_{\rm FLD,i}\}$, cf. Eq. (26b) with $\alpha \approx 0.5$.

C2 Tangent-ray Boltzmann-solver

For calculating the reference solution in Sec. 4.3.1 we employ a time-independent tangent-ray variable-Eddington-factor (TR-VEF) scheme closely analog to what is described in Chap. 83 of Mihalas & Mihalas (1984) and in Rampp & Janka (2002). For the discretization of the two-moment system (cf. Eqs. (7) with $\partial_t = 0$, $\boldsymbol{v} = 0$ and the source terms expressed as in Eq. (14)) we use a finite-difference scheme in which we interprete the energy densities $\hat{E}_{\mathsf{i}}$ to be located at cell centers and the flux densities $\hat{F}_{\mathsf{i}+\frac{1}{2}}$ to be located at cell interfaces. Using first-order differences for the radial derivatives, this leads to the following linear system of equations:

$$\frac{\hat{F}_{\mathsf{i}+\frac{1}{2}} - \hat{F}_{\mathsf{i}-\frac{1}{2}}}{\Delta r_{\mathsf{i}}} + \frac{2\hat{F}_{\mathsf{i}}}{r_{\mathsf{i}}} + c\hat{\kappa}_{\rm a,i}\hat{E}_{\mathsf{i}} = c\hat{\kappa}_{\rm a,i}\hat{E}^{\rm eq}_{\mathsf{i}}\,, \tag{C4a}$$

$$\frac{\hat{\chi}_{\mathsf{i}+1}\hat{E}_{\mathsf{i}+1} - \hat{\chi}_{\mathsf{i}}\hat{E}_{\mathsf{i}}}{\Delta r_{\mathsf{i}+\frac{1}{2}}} + \frac{\hat{E}_{\mathsf{i}+\frac{1}{2}}}{r_{\mathsf{i}+\frac{1}{2}}}\left(3\hat{\chi}_{\mathsf{i}+\frac{1}{2}} - 1\right) + c\hat{\kappa}_{\rm tra,i+\frac{1}{2}}\hat{F}_{\mathsf{i}+\frac{1}{2}} = 0 \tag{C4b}$$

for $\mathsf{i} = 1, \ldots, N_r$, where $\Delta r_{\mathsf{i}+\frac{1}{2}} \equiv r_{\mathsf{i}+1} - r_{\mathsf{i}}$ and $\hat{E}_{\mathsf{i}+\frac{1}{2}}, \hat{F}_{\mathsf{i}}$ are linear interpolations of the nearest neighbors on the corresponding staggered grid. The Eddington factors χ required to solve Eqs. (C4) have to be obtained from the Boltzmann equation. For the considered type of interactions, the latter reads (e.g. Cernohorsky et al. 1989)

$$\mu\partial_r\mathcal{I}(r,\mu) + \frac{1-\mu^2}{r}\partial_\mu\mathcal{I}(r,\mu) = \kappa_{\rm a}\mathcal{I}^{\rm eq} + \frac{1}{4\pi}\left(\kappa^0_{\rm s}\, c\, E + \kappa^1_{\rm s}\,\mu\, F\right) - (\kappa_{\rm a} + \kappa^0_{\rm s})\mathcal{I}(r,\mu)\,, \tag{C5}$$

where μ is the cosine of the angle between the radial direction and the direction of neutrinos in momentum space, $\mathcal{I}^{\rm eq}$ is the specific intensity corresponding to neutrinos being in thermal equilibrium, and the scattering opacity $\kappa_{\rm s} = \kappa^0_{\rm s} - \kappa^1_{\rm s}/3$ is decomposed into an isotropic (superscript "0") and an anisotropic (superscript "1") contribution. For solving Eq. (C5) we first make a change of variables $(r,\mu) \to (s \equiv \mu\, r, p \equiv \sqrt{1-\mu^2}r)$ and we use

$$j(s,p) \equiv (\mathcal{I}(\mu) + \mathcal{I}(-\mu))/2\,, \tag{C6a}$$

$$h(s,p) \equiv (\mathcal{I}(\mu) - \mathcal{I}(-\mu))/2 \tag{C6b}$$

to rewrite Eq. (C5) into the following system of equations

$$\partial_s h(s,p) + (\kappa_{\rm a} + \kappa^0_{\rm s})j(s,p) = \kappa_{\rm a}\mathcal{I}^{\rm eq} + \kappa^0_{\rm s}\frac{c}{4\pi}\,E\,, \tag{C7a}$$

$$\partial_s j(s,p) + (\kappa_{\rm a} + \kappa^0_{\rm s})h(s,p) = \kappa^1_{\rm s}\frac{c}{4\pi}\,\mu\, F. \tag{C7b}$$

Equations (C7) are independently solved along each tangent-ray characterized by a constant impact parameter $p_{\mathsf{i}} = r_{\mathsf{i}}$ ($\mathsf{i} = 1, \ldots, N_r$). We employ a finite-difference prescription in which we interprete $\hat{j}_{\mathsf{i}}$ to be located at cell centers and $\hat{h}_{\mathsf{i}+\frac{1}{2}}$ to be located at cell interfaces of the corresponding tangent-ray grid. The linear system of difference equations to be solved then follows in an analog fashion as for the two-moment system, cf. Eq. (C4). For the numerical angular integration of the specific intensity we use the quadrature weights of Yorke (1980).

In practice, we obtain the initial values of χ by solving the Boltzmann equation with $E = F = 0$. Subsequently, the two-moment system and the Boltzmann equation are iteratively solved until convergence is achieved.